

# Proto-neutron stars with heavy baryons and universal relations

Adriana R. Raduta<sup>1\*</sup>, Micaela Oertel<sup>2†</sup> and Armen Sedrakian<sup>3,4‡</sup>

<sup>1</sup>*National Institute for Physics and Nuclear Engineering (IFIN-HH), RO-077125 Bucharest, Romania*

<sup>2</sup>*LUTH, Observatoire de Paris, Université PSL, CNRS, Université de Paris, 92195 Meudon, France*

<sup>3</sup>*Frankfurt Institute for Advanced Studies, D-60438 Frankfurt-Main, Germany*

<sup>4</sup>*Institute of Theoretical Physics, University of Wrocław, 50-204 Wrocław, Poland*

4 August 2020

## ABSTRACT

We use covariant density functional theory to obtain the equation of state (EoS) of matter in compact stars at non-zero temperature, including the full baryon octet as well as the  $\Delta(1232)$  resonance states. Global properties of hot  $\Delta$ -admixed hypernuclear stars are computed for fixed values of entropy per baryon ( $S/A$ ) and lepton fraction ( $Y_L$ ). Universal relations between the moment of inertia, quadrupole moment, tidal deformability, and compactness of compact stars are established for fixed values of  $S/A$  and  $Y_L$  that are analogous to those known for cold catalyzed compact stars. We also verify that the  $I$ -Love- $Q$  relations hold at finite temperature for constant values of  $S/A$  and  $Y_L$ .

## 1 INTRODUCTION

Cold, mature compact stars are well described by a one-parameter equation of state (EoS) relating pressure to (energy) density. In contrast, the studies of the dynamics of core-collapse supernovae (CCSN) (Janka et al. 2007; Mezzacappa et al. 2015; O’Connor & Couch 2018; Burrows et al. 2020), proto-neutron star (PNS) evolution (Pons et al. 1999), stellar black-hole (BH) formation (Sumiyoshi et al. 2007; Fischer et al. 2009; O’Connor & Ott 2011; Hempel et al. 2012) and binary neutron star (BNS) mergers (Shibata & Taniguchi 2011; Rosswog 2015; Baiotti & Rezzolla 2017; Ruiz et al. 2020) require as an input an EoS at non-zero temperature and out of (weak)  $\beta$ -equilibrium, *i.e.*, the pressure becomes a function of three thermodynamic parameters. For describing all of the above mentioned astrophysical scenarios one needs to consider baryon number densities,  $n_B$ , ranging from sub-saturation densities up to several times the nuclear saturation density  $n_s \simeq 0.16 \text{ fm}^{-3}$ , temperatures up to 100 MeV and charge fractions  $0 \leq Y_Q = n_Q/n_B \leq 0.6$ , where  $n_Q$  is defined as the total hadronic charge density (Oertel et al. 2017).

In recent years the EoS of cold compact stars has been considerably constrained due to several new astrophysical observations (compact star masses, radii and tidal deformability), information coming from experimental nuclear physics and the progress in *ab-initio* calculations of pure neutron matter. The new data has, in particular, narrowed the possible parameter space of EoS derived from density functional theory (DFT). There exist a large number of DFT based EoS which are applicable to cold  $\beta$ -equilibrated neutron stars, see *e.g.* (Weissenborn et al. 2012b,a; Colucci & Sedrakian 2013; van Dalen et al. 2014; Oertel et al. 2015; Chatterjee & Vidana 2016; Fortin et al.

2016; Chen et al. 2007; Drago et al. 2014; Cai et al. 2015; Zhu et al. 2016; Sahoo et al. 2018; Kolomeitsev et al. 2017; Li et al. 2018; Li & Sedrakian 2019b; Ribes et al. 2019; Li et al. 2020). The latter works address, in particular, the problem of hyperonization of dense matter (*the hyperon puzzle*) and the possible emergence of  $\Delta$ -degrees of freedom in dense matter at zero temperature. Models of finite temperature dense matter with heavy baryon degrees of freedom, applicable to CCSN and BNS mergers, which are consistent with the constraints imposed by modern data are less numerous, see (Oertel et al. 2012; Colucci & Sedrakian 2013; Oertel et al. 2016; Marques et al. 2017; Dexheimer 2017; Fortin et al. 2018; Malfatti et al. 2019; Stone et al. 2019).

The first aim of this work is to obtain an EoS of non-zero temperature matter, which is well-constrained by astrophysics and laboratory data, on the basis of the DDME2 parameterisation (Lalazissis et al. 2005) extended to hypernuclear matter by Fortin et al. (2016)<sup>1</sup>. We include additionally the  $\Delta$  degrees of freedom as they add an important feature: they soften the EoS in an intermediate density range, reduce the compact star radii for intermediate masses (Drago et al. 2014; Li et al. 2018) which improves the agreement between theoretical models and observations. The resulting finite-temperature EoS are relevant for the variety of above mentioned astrophysical scenarios, which are known to depend sensitively on the EoS (Pons et al. 1999; Sekiguchi et al. 2011; Bauswein et al. 2012; Fischer et al. 2014; Perego et al. 2019; Peres et al. 2013; Schneider et al.

<sup>1</sup> Similar extensions of the DDME2 parameterisation to the hyperonic sector, which differs in the way the parameters in the scalar-meson sector are fixed, can be found in Colucci & Sedrakian (2013); van Dalen et al. (2014); Li et al. (2018).

2019; Bauswein 2019; Schneider et al. 2020; Yasin et al. 2020).

To illustrate the properties of the EoS and the impact of heavy baryons, we make calculations for constant values of entropy per baryon  $S/A$  ( $0 \leq S/A \leq 4$ ) either assuming constant lepton fraction  $Y_L$  ( $0.2 \leq Y_L \leq 0.4$ ) in the neutrino-trapped regime or freely streaming neutrinos and matter in  $\beta$ -equilibrium. Some of the considered thermodynamic conditions are relevant for different stages in the evolution from a PNS to a compact star (Burrows & Lattimer 1986; Prakash et al. 1997; Pons et al. 1999). Broad coverage of all the astrophysics relevant parameter space will be given elsewhere. Under the conditions of PNS, the neutrinos are trapped and the lepton fraction is thus given by the sum of charged leptons and neutrinos fractions. For each set of thermodynamic conditions, we will discuss properties of the EoS and matter composition as well as maximum mass and radii of hot stars. Possible instability windows of non-accreting PNS with respect to collapse to a BH is investigated following Bombaci (1996). The maximum gravitational mass at constant  $S/A$ , assuming neutrino-transparent  $\beta$ -equilibrated matter, is related to the collapse to a BH during in failed CCSNe (Schneider et al. 2020). We study here the influence of heavy baryons on this maximum mass.

The second motivation of this study is to test the universal relations among the global properties of stationary, slowly and rigidly rotating compact stars at finite temperature. In essence, universality means that these relations, well established at zero temperature, are *independent of the underlying EoS* (Yagi & Yunes 2013a; Maselli et al. 2013; Breu & Rezzolla 2016; Yagi & Yunes 2017; Paschalidis et al. 2018) and are thus very helpful for the interpretation of observational data since they allow to mitigate the uncertainties related to the EoS. Given the importance of such relations, it is interesting to investigate them under new conditions, such as finite temperatures and out-of-equilibrium with respect to weak interactions.

The possibility of some of these relations being universal at finite temperature has been studied before (Martinon et al. 2014; Marques et al. 2017; Lenka et al. 2019). The moment of inertia as a function of compactness was studied by Lenka et al. (2019), who concluded that thermal effects lead to deviations from the universal relations obtained for  $\beta$ -equilibrated matter at zero temperature. Similar conclusions have been reached for the so-called  $I$ –Love– $Q$  relations, where again it was claimed that at finite temperature deviations from the zero-temperature universality are found (Martinon et al. 2014; Marques et al. 2017). Below we show that, if one considers fixed values of  $(S/A, Y_{L,e})$ , where  $Y_{L,e}$  is the electron fraction, the  $\bar{I} - \bar{\lambda}$  and  $\bar{I} - \bar{Q}$  relations are universal to accuracy comparable to that obtained for cold compact stars. The same is true for several global properties of compact stars, such as the moment of inertia, quadrupole moment, tidal deformability as function of compactness. Only the binding energy per unit of the gravitational mass shows deviations from universality.

This paper is organized as follows. In Sec. 2 we describe the details of the parameterisation that has been used in modeling the EoS from relativistic density functional theory. Section 3 is devoted to the discussion of the results for the mass and radius of hot compact stars. In Section 4.1 we investigate the behavior of different (normalised) global

properties as a function of the star’s compactness. Section 4.2 focuses on  $I$ –Love– $Q$  relations. We conclude in Sec. 5. Throughout this paper we use the natural units with  $c = \hbar = k_B = G = 1$ .

## 2 THE MODEL

We consider matter at non-zero temperature as it occurs in CCSN, PNS and BNS mergers. Leptons (electrons, muons and neutrinos) and photons are considered as non-interacting gases, whereas under the relevant conditions, the tau lepton can safely be neglected. The partition function of the system thus factorizes into a product of baryonic (index  $B$ ), leptonic (index  $L$ ) and photonic ( $\gamma$ ) partition functions:  $\mathcal{Z} = \mathcal{Z}_B \mathcal{Z}_L \mathcal{Z}_\gamma$ . In thermodynamic equilibrium, within the grand-canonical ensemble,

$$\begin{aligned} \frac{1}{V} \ln \mathcal{Z}_L &= \sum_j g_j \int \frac{d^3 k}{(2\pi)^3} \frac{k^2}{\varepsilon_j(k)} \\ &\quad [f_{\text{FD}}(\varepsilon_j(k) - \mu_j) + f_{\text{FD}}(\varepsilon_j(k) + \mu_j)], \quad (1) \\ \frac{1}{V} \ln \mathcal{Z}_\gamma &= g_\gamma \int \frac{d^3 k}{(2\pi)^3} \frac{k^2}{\varepsilon_\gamma(k)} f_{\text{BE}}(\varepsilon_\gamma(k)). \quad (2) \end{aligned}$$

where  $f_{\text{FD}}$  and  $f_{\text{BE}}$  are the Fermi-Dirac and Bose-Einstein distribution functions at temperature  $T$ , respectively,  $g_j = (2s_j + 1)$  is the spin degeneracy factor with  $s_j$  being the lepton’s spin [ $g_j = 2$  for charged leptons and  $g_j = 1$  for (left-handed) neutrinos] and  $\varepsilon_j(k)$  and  $\mu_j$  are the single particle energy and the chemical potential of the lepton  $j$ . In Eq. (2)  $g_\gamma = 2$  and  $\varepsilon_\gamma(k)$  are the photon spin degeneracy and energy. The partition function of the strongly interacting baryons requires a model of the strong nuclear interaction. Within the relativistic density functional theory it is given by a sum of kinetic part (which has a form analogous to that of an ideal gas) and a potential term. We write it as

$$\begin{aligned} \frac{1}{V} \ln \mathcal{Z}_B &= \frac{1}{V} \ln \mathcal{Z}_m + \sum_{i \in \text{baryons}} \frac{2J_i + 1}{3} \int \frac{d^3 k}{(2\pi)^3} \frac{k^2}{E_i(k)} \\ &\quad \cdot [f_{\text{FD}}(E_i(k) - \mu_i^*) + f_{\text{FD}}(E_i(k) + \mu_i^*)], \quad (3) \end{aligned}$$

where  $(2J_i + 1)$  denotes the spin degeneracy factor,  $E_i = \sqrt{k^2 + M_i^{*2}}$  is the single-particle energy. Interactions enter via the effective masses  $M_i^*$  and effective chemical potentials  $\mu_i^*$ . The potential term is given by

$$\frac{T}{V} \ln \mathcal{Z}_m = -\frac{1}{2} m_\sigma^2 \bar{\sigma}^2 + \frac{1}{2} m_\omega^2 \bar{\omega}^2 + \frac{1}{2} m_\rho^2 \bar{\rho}^2 + \frac{1}{2} m_\phi^2 \bar{\phi}^2. \quad (4)$$

The values of the mean-fields having the quantum numbers of the corresponding mesons, are determined by

$$m_\sigma^2 \bar{\sigma} = \sum_i g_{\sigma i} n_i^s, \quad (5a)$$

$$m_\omega^2 \bar{\omega} = \sum_i g_{\omega i} n_i, \quad (5b)$$

$$m_\phi^2 \bar{\phi} = \sum_i g_{\phi i} n_i, \quad (5c)$$

$$m_\rho^2 \bar{\rho} = \sum_i g_{\rho i} t_{3i} n_i, \quad (5d)$$

where  $t_{3i}$  is the third component of isospin of baryon  $i$ ,  $n_i^s$  and  $n_i$  are the scalar and the number density. These are

given by

$$n_i^s = \frac{1}{\pi^2} \int \frac{k^2 M_i^*}{E_i(k)} [f_{\text{FD}}(E_i(k) - \mu_i^*) + f_{\text{FD}}(E_i(k) + \mu_i^*)] dk, \quad (6)$$

$$n_i = \frac{1}{\pi^2} \int k^2 [f_{\text{FD}}(E_i(k) - \mu_i^*) - f_{\text{FD}}(E_i(k) + \mu_i^*)] dk. \quad (7)$$

Note that Eq. (4) does not contain mesonic self-interactions, as is the case of many DFT models. Here, we employ instead a model belonging to the subclass of DFTs which allow for density-dependent couplings,  $g_{m,B}(n_B) = g_{m,B}(n_s)h_m(x)$  with  $x = n_B/n_s$ , where  $n_s$  is the nuclear saturation density. We will further assume that the couplings of mesons to hyperons and  $\Delta$ -resonances have the same density dependence as those to nucleons. The effective chemical potentials are given by

$$\mu_i^* = \mu_i - g_{\omega i} \bar{\omega} - g_{\rho i} t_{3i} \bar{\rho} - g_{\phi i} \bar{\phi} - \Sigma_0^R, \quad (8)$$

where

$$\Sigma_0^R = \sum_i \left( \frac{\partial g_{\omega i}}{\partial n_i} \bar{\omega} n_i + t_{3i} \frac{\partial g_{\rho i}}{\partial n_i} \bar{\rho} n_i + \frac{\partial g_{\phi i}}{\partial n_i} \bar{\phi} n_i - \frac{\partial g_{\sigma i}}{\partial n_i} \bar{\sigma} n_i^s \right), \quad (9)$$

is the rearrangement term. The effective baryon masses depend on the scalar mean field according to

$$M_i^* = M_i - g_{\sigma i} \bar{\sigma}. \quad (10)$$

From the partition function one obtains pressure, entropy density, energy density, and particle number densities in a standard fashion

$$P = \frac{T}{V} \ln \mathcal{Z}, \quad (11)$$

$$s = \frac{1}{V} \left. \frac{\partial (T \ln \mathcal{Z})}{\partial T} \right|_{V, \{\mu_i\}}, \quad (12)$$

$$e = -\frac{T}{V} \ln \mathcal{Z} + \sum_i \mu_i n_i + Ts, \quad (13)$$

$$n_i = \frac{1}{V} \left. \frac{\partial (T \ln \mathcal{Z})}{\partial \mu_i} \right|_{V, T}. \quad (14)$$

Note that each component contributes additively to the net thermodynamic quantity of interest, which is easy to see by substituting Eqs. (1)-(3) in Eqs. (11)-(13).

In this work, we use the density-dependent DDME2 parameterisation for the nucleonic sector (Lalazissis et al. 2005) and its extension to the hyperonic sector by Fortin et al. (2016), which fixes the hyperonic couplings in the vector meson sector to the values implied by the  $SU(6)$  symmetric quark model and adjusts the scalar couplings to the depth of the hyperon potentials in nuclear matter at saturation. Alternative extensions of the DDME2 model to the baryonic octet have been carried out and applied to compact stars elsewhere (Colucci & Sedrakian 2013; van Dalen et al. 2014; Fortin et al. 2017; Li et al. 2018). The differences between the models reside in the choice of the different hyperonic couplings, which are not well constrained. In addition to hyperons, we include the  $\Delta(1232)$  resonance states of the baryon  $J^{3/2}$ -decouplet, which were brought recently into focus in the context of compact stars by several groups (Chen et al. 2007; Drago et al. 2014; Cai et al. 2015; Zhu et al. 2016; Sahoo et al. 2018; Kolomeitsev et al. 2017; Li et al. 2018; Li et al. 2020; Li & Sedrakian 2019b; Ribes et al. 2019).

Model	$n_s$ [fm $^{-3}$ ]	$E_s$ [MeV]	$K_{\text{inf}}$ [MeV]	$J$ [MeV]	$L$ [MeV]	$K_{\text{sym}}$ [MeV]
DDME2	0.152	-16.1	250.9	32.3	51.2	-87.1

**Table 1.** Key nuclear matter properties of the DDME2 model (Lalazissis et al. 2005): the binding energy per nucleon ( $E_s$ ) and compression modulus ( $K_{\text{inf}}$ ) of symmetric nuclear matter at saturation density ( $n_s$ ) together with the symmetry energy ( $J$ ), its slope ( $L$ ) and curvature ( $K_{\text{sym}}$ ).

Our choice of the nucleonic DDME2 EoS is motivated by the following factors: i) the parameters of isospin symmetric (*i.e.* equal numbers of protons and neutrons) nuclear matter around saturation density are in good agreement with present experimental constraints (Lalazissis et al. 2005) (see Table 1); ii) the properties of atomic nuclei, such as binding energies, rms radii of charge distribution, neutron skin thickness, quadrupole and hexadecupole moments of heavy and superheavy nuclei, excitation energies of the iso-scalar giant monopole- and iso-vector giant dipole-resonances in spherical nuclei, are in good agreement with experimental values (Lalazissis et al. 2005); iii) the energy per baryon of low-density neutron matter predicted by the DDME2 functional is in good agreement with that from *ab initio* calculations (Gandolfi et al. 2012; Hebeler et al. 2013) [see Fig. 12 in (Fortin et al. 2016) and Fig. 1 in (Li & Sedrakian 2019a)]. Point (iii) implies that the model predicts a relatively low value for the slope of the symmetry energy  $L$ , which lies within the domains  $40 \lesssim L \lesssim 62$  MeV (Lattimer & Steiner 2014) or  $30 \lesssim L \lesssim 86$  MeV (Oertel et al. 2017) deduced from experiments [see Fig. 13 in Fortin et al. (2016)]. The curvature of the symmetry energy falls in the intervals  $K_{\text{sym}} = -111.8 \pm 71.3$  MeV (Mondal et al. 2017),  $K_{\text{sym}} = -85_{-70}^{+82}$  MeV (Baillot d’Etivaux et al. 2019) and  $K_{\text{sym}} = -102 \pm 71$  MeV (Zimmerman et al. 2020), which were obtained from the analyses of different nuclear and compact star properties. This implies that the DDME2 parameterisation has a reasonable behavior in the isovector channel.

The extension of the DDME2 to the hyperonic sector by Fortin et al. (2016) –labelled hereafter “DDME2Y”– assumes  $SU(6)$  flavor symmetry for the vector meson-hyperonic couplings and adjusts the couplings of the scalar  $\sigma$ -meson to hyperons to reproduce the empirical depths of the hyperon potentials in symmetric nuclear matter at saturation. The potential for particle  $j$  in  $k$ -particle matter is thereby defined via the effective masses and chemical potentials as

$$U_j^{(k)}(n_k) = M_j^* - M_j + \mu_j - \mu_j^*. \quad (15)$$

The DDME2Y parameterisation uses the values  $U_\Lambda^{(N)} \approx -28$  MeV,  $U_\Xi^{(N)} \approx -14$  MeV,  $U_\Sigma^{(N)} \approx 30$  MeV in isospin symmetric nuclear matter (Gal et al. 2016). Coupling constants of the hyperons  $Y$  to the meson fields are customarily expressed in terms of the coupling constants of the nucleons  $N$  to the meson fields,  $x_{m,Y} = g_{m,Y}/g_{m,N}$ , where  $m \in \sigma, \rho, \omega$ , etc. labels the meson. Adopting this convention, DDME2Y parameterisation is defined by the following coupling constants:  $x_{\sigma\Lambda} = 0.615$ ,  $x_{\sigma\Xi} = 0.3225$ ,  $x_{\sigma\Sigma} = 0.47$ ,  $x_{\omega\Lambda} = 2/3$ ,  $x_{\omega\Xi} = 1/3$ ,  $x_{\omega\Sigma} = 2/3$ ,  $x_{\rho\Lambda} = 0$ ,  $x_{\rho\Xi} = 1$ ,  $x_{\rho\Sigma} = 2$ . The coupling constants of the hidden strangeness meson  $\phi$  to the

baryons are  $g_{\phi N}=0$ ,  $g_{\phi\Lambda} = -\sqrt{2}/3g_{\omega N}$ ,  $g_{\phi\Sigma} = -2\sqrt{2}/3g_{\omega N}$ ,  $g_{\phi\Xi} = -\sqrt{2}/3g_{\omega N}$ .

The DDME2Y parameterisation above fulfills not only the existing constraints from terrestrial experiments and *ab initio* calculations, but it is in agreement with existing compact star observations as well (see Section 3 and Table 2). Specifically, the predicted value of the compact star maximum mass exceeds the observational lower bound on the maximum mass of a compact star  $2M_{\odot}$  (Demorest et al. 2010; Antoniadis et al. 2013; Arzoumanian et al. 2018). Furthermore, the predicted value of the radius of the canonical  $1.4M_{\odot}$  compact star is in agreement with the recent inferences  $R = 13.02_{-1.06}^{+1.24}$  km (Miller et al. 2019) and  $R = 12.71_{-1.19}^{+1.14}$  km (Riley et al. 2019) from the data obtained by the NICER mission. The tidal deformability for a  $1.4M_{\odot}$  compact star is  $\Lambda_{1.4} = 712$ . This value lies outside the range  $\Lambda_{1.4} = 190_{-120}^{+390}$  (Abbott et al. 2018) and at the upper limit of the interval  $300_{-230}^{+420}$  (Abbott et al. 2019) extracted, at a 90% confidence level, from the analysis of the GW170817 event. Note that the values of tidal deformability in Abbott et al. (2018) have been obtained assuming that both compact objects are NSs obeying a common equation of state; on the other hand, the values in Abbott et al. (2019) have been obtained, as in the initial analysis of GW170817 event (Abbott et al. 2017), by making minimal assumptions about the nature of the compact objects and allowing the tidal deformability of each object to vary independently.

The masses of  $\Delta$ -resonances, which form an isospin quadruplet, lie between those of  $\Sigma$  and  $\Xi$  hyperons, therefore they are expected to nucleate in dense stellar matter according to the same energetic arguments employed for the nucleation of hyperons (Glendenning 1985). While in the vacuum  $\Delta$ s are broad resonances which decay into nucleons with emission of a pion, in stellar matter they are thought to be stabilised by the Pauli-blocking of the final nucleon states. Apart from the narrowing the quasi-particle width of the  $\Delta$ s, matter effects may shift the quasi-particle energy to larger values (Sawyer 1972; Ouellette 2011), which would suppress the  $\Delta$  degrees of freedom. Below, we will assume that the  $\Delta$ s retain their vacuum masses and have negligible width, as has been done in the recent literature (Chen et al. 2007; Drago et al. 2014; Cai et al. 2015; Zhu et al. 2016; Sahoo et al. 2018; Kolomeitsev et al. 2017; Li et al. 2018; Li et al. 2020; Li & Sedrakian 2019b; Ribes et al. 2019).

The information about nucleon- $\Delta$  interaction is extracted from pion-nucleus scattering and pion photo-production (Nakamura et al. 2010), electron scattering on nuclei (Koch & Ohtsuka 1985) and electromagnetic excitations of the  $\Delta$ -baryons (Wehrberger et al. 1989). As reviewed by Drago et al. (2014) and Kolomeitsev et al. (2017) (a) the potential of the  $\Delta$  in the nuclear medium is slightly more attractive than the nucleon potential  $-30$  MeV +  $U_N^{(N)} \lesssim U_{\Delta}^{(N)} \lesssim U_N^{(N)}$ , which translates in values of  $x_{\sigma\Delta}$  slightly larger than 1, (b)  $0 \lesssim x_{\sigma\Delta} - x_{\omega\Delta} \lesssim 0.2$  and (c) no experimental constraints exist for the value of  $x_{\rho\Delta}$ .

Since there remain large uncertainties on the values of the  $\Delta$  couplings, they are commonly varied in a certain plausible range. Previous works employed the ranges  $0.85 \lesssim x_{\sigma\Delta} \lesssim 1.15$ ,  $0.6 \lesssim x_{\omega\Delta} \lesssim 1.2$ , and  $0.5 \lesssim x_{\rho\Delta} \lesssim 3$  (Chen et al. 2007; Drago et al. 2014; Cai et al. 2015; Zhu et al. 2016; Sahoo et al. 2018; Kolomeitsev et al.

2017; Li et al. 2018; Li et al. 2020; Li & Sedrakian 2019b; Ribes et al. 2019). Furthermore, it was shown that:

- small values of  $x_{\sigma\Delta}$  (which lead to small values  $U_{\Delta}^{(N)}$ ) result in larger values of compact star radii (Zhu et al. 2016; Kolomeitsev et al. 2017; Spinella 2017; Li et al. 2018); the effect on the maximum mass is small and dependent on the high density part of the nucleonic EoS,
- small values of  $x_{\omega\Delta}$  and  $x_{\rho\Delta}$  imply lower values of compact star radii and maximum masses (Drago et al. 2014; Cai et al. 2015; Sahoo et al. 2018; Li et al. 2020; Li & Sedrakian 2019b; Ribes et al. 2019),
- the threshold density for the onset of  $\Delta$  is correlated with  $x_{\sigma\Delta}$  (Zhu et al. 2016; Kolomeitsev et al. 2017; Spinella 2017; Li et al. 2018),  $x_{\rho\Delta}$  (Cai et al. 2015; Zhu et al. 2016; Sahoo et al. 2018),  $x_{\omega\Delta}$  (Ribes et al. 2019) and the  $\Delta$ -effective mass (Cai et al. 2015; Sahoo et al. 2018),
- The effective mass of  $\Delta$ s significantly impacts compact star radii and maximum masses (Cai et al. 2015; Sahoo et al. 2018),
- the threshold density for the onset of  $\Delta$  strongly depends on the slope of the symmetry energy at saturation (Drago et al. 2014; Cai et al. 2015). Cai et al. (2015) also showed that it is less sensitive to the other parameters of symmetric saturated nuclear matter.

The appearance of  $\Delta$  resonances in hot stellar matter with fixed lepton fraction was investigated only recently by Malfatti et al. (2019). It was found that: (i) the lower the lepton fraction, the higher the  $\Delta$  abundances; (ii) at high enough temperatures and densities the four isobars are populated in addition to all hyperonic degrees of freedom; (iii) the most abundant of the  $\Delta$ -isobars is  $\Delta^{-}$ .

In this work, we use the following values of the couplings of mesons to  $\Delta$ s:  $x_{\sigma\Delta} = 1.1$ , which corresponds to a  $\Delta$  potential at the saturation  $U_{\Delta}^{(N)} \approx -83$  MeV,  $x_{\omega\Delta} = 1.1$ , and  $x_{\rho\Delta} = 1.0$  and  $x_{\phi\Delta} = 0$ . In the following this model will be referred to as DDME2Y $\Delta$ .

We assume strangeness changing weak equilibrium leading to the following equilibrium conditions,

$$\mu_{\Lambda} = \mu_{\Sigma^0} = \mu_{\Xi^0} = \mu_{\Delta^0} = \mu_n = \mu_B; \quad (16)$$

$$\mu_{\Sigma^-} = \mu_{\Xi^-} = \mu_{\Delta^-} = \mu_B - \mu_Q; \quad (17)$$

$$\mu_{\Sigma^+} = \mu_{\Delta^+} = \mu_B + \mu_Q; \quad (18)$$

$$\mu_{\Delta^{++}} = \mu_B + 2\mu_Q, \quad (19)$$

where  $\mu_B$  is the baryon number chemical potential and  $\mu_Q = \mu_p - \mu_n$  is the charge chemical potential. The equilibrium conditions, Eqs. (16)-(19), together with the total baryonic charge  $n_p + n_{\Sigma^+} + 2n_{\Delta^{++}} + n_{\Delta^+} - (n_{\Sigma^-} + n_{\Xi^-} + n_{\Delta^-}) = n_Q$  determine the composition of baryonic matter for a given  $(n_B, T, Y_Q = n_Q/n_B)$ . The requirement of global electrical charge neutrality of stellar matter then fixes the charged lepton density  $Y_Q = Y_e + Y_{\mu}$  where  $Y_e = (n_{e^-} - n_{e^+})/n_B$  and  $Y_{\mu} = (n_{\mu^-} - n_{\mu^+})/n_B$ . For free-streaming neutrinos  $\mu_e = \mu_{\mu} = -\mu_Q$ , whereas for trapped neutrinos  $\mu_{e/\mu} = \mu_{L,e/\mu} - \mu_Q$ , where  $\mu_{L,e/\mu}$  denotes the (electron/muon) lepton number chemical potential. The lepton  $Y_{L,e/\mu}$  fractions, which are conserved separately, are then defined via the total lepton number density divided by  $n_B$ . Throughout this paper “ $\beta$ -equilibrium” refers to  $\beta$ -equilibrated matter which, in addition, is transparent to neutrinos. This means that

the corresponding lepton number chemical potentials vanish  $\mu_{L,e} = \mu_{L,\mu} = 0$ .

At densities below nuclear saturation density and not too high temperature, the matter becomes unstable towards density fluctuations, because of the competition between nuclear and Coulomb interactions. As a consequence, a large variety of clusters are formed, all of which are in chemical and thermal equilibrium with the unbound baryons. If the temperature is high enough, hyperons and  $\Delta$ s are in principle expected to nucleate within the clusters and unbound components as well, but for simplicity, we neglect this possibility here. The theoretical framework suitable under these conditions is the Nuclear Statistical Equilibrium (NSE) (Hempel & Schaffner-Bielich 2010; Raduta & Gulminelli 2010; Gulminelli & Raduta 2015). Interactions among unbound particles and clusters are usually accounted for in the excluded volume approximation, while those in the homogeneous matter within a chosen mean-field approach. The transition between the inhomogeneous and homogeneous phases is in principle realized by minimizing, for equal values of the intensive thermodynamic observables, the relevant thermodynamic potential. The EoS used in our work are obtained by smoothly merging the uniform matter EoS to the NSE model HS(DD2) (Hempel & Schaffner-Bielich 2010) for inhomogeneous matter. The latter is publicly available on the Compose database<sup>2</sup> (Typel et al. 2015). In principle, the transition density depends on the EoS, temperature and charge fraction, see e.g. the discussion in (Ducoin et al. 2008, 2007; Pais et al. 2010), but for simplicity, the matching is performed here at a fixed transition density  $n_t = n_s/2$ . Inhomogeneous and homogeneous matter are considered at the same  $S/A$  and  $Y_{L,e}/\mu_{L,e}$ . The similarity between the effective interactions of DDME2 (Lalazissis et al. 2005) and DD2 (Typel et al. 2010) leads to a coherent treatment of the EoS over the whole density regime and the fixed transition density only induces very small thermodynamic inconsistencies with little impact on the EoS and the global star properties studied here.

### 3 EQUATION OF STATE AND COMPOSITION

A PNS is born in the aftermath of a successful supernova explosion, when the stellar remnant and the expanding ejecta get gravitationally decoupled. The evolutionary epoch during which the remnant changes from a hot and lepton-rich PNS to a cold and deleptonized compact star lasts for several tens of seconds and consists of two major evolutionary stages (Prakash et al. 1997; Pons et al. 1999): the deleptonization stage and the cooling stage. The deleptonization stage is characterized by a gradual decrease of the net lepton and proton fractions and the heat-up of the core, due to the diffusion of trapped electron neutrinos from the central region outward. The cooling stage is characterized by a simultaneous decrease of both entropy and lepton content. The structure and composition of the PNS during this epoch will be investigated here in a schematic way, assuming entropy per baryon and lepton fraction with typical

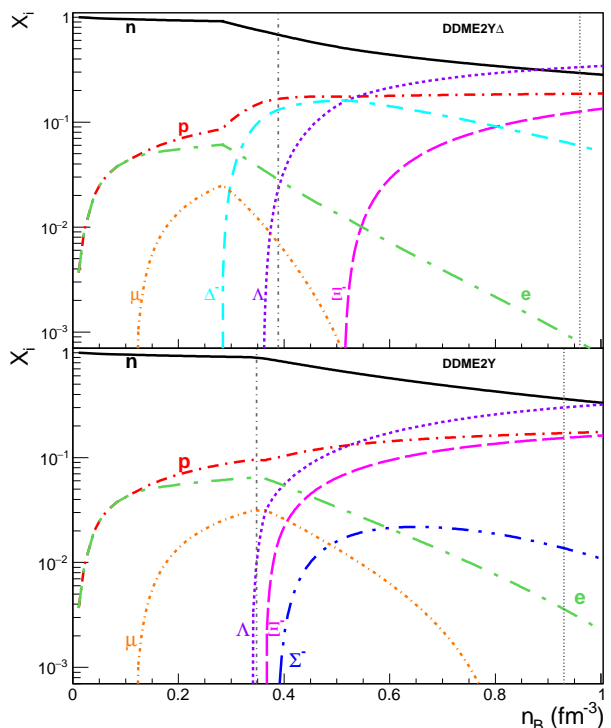


**Figure 1.** Relative abundances in  $\beta$ -equilibrated, neutrino-transparent, cold compact star matter as predicted by DDME2Y (bottom panel) and DDME2Y $\Delta$  (top panel) models as function of baryon number density. Note that the nucleation of  $\Delta^-$  resonance leads to a suppression of  $\Sigma^-$  abundance. Thin vertical lines mark the central baryon number densities corresponding to a  $1.44M_\odot$  star (dot-dashed) and the maximum mass star (dotted), respectively.

values (Prakash et al. 1997; Pons et al. 1999): ( $S/A = 1$ ,  $Y_{L,e} = 0.4$ ), ( $S/A = 2$ ,  $Y_{L,e} = 0.2$ ), ( $S/A = 1$ ,  $\mu_{L,e}/\mu = 0$ ) and ( $S/A = 0$ ,  $\mu_{L,e}/\mu = 0$ ).

#### 3.1 Composition

Fig. 1 shows relative particle abundances as a function of baryon number density in cold  $\beta$ -equilibrated compact star matter. Results corresponding to baryonic matter composed of  $NY\Delta$  (top panel) are compared with those corresponding to  $NY$  (bottom panel). In both cases, the net charge neutrality is guaranteed by electrons and muons. In the case of  $NY$  matter, the only non-nucleonic baryonic degrees of freedom that nucleate in stable stars are  $\Lambda$ ,  $\Xi^-$  and  $\Sigma^-$ , as already discussed elsewhere (Fortin et al. 2016; Raduta et al. 2018). This can be explained by the large negative charge chemical potential in matter featuring low charge fractions favoring negatively charged particles. Under the considered conditions, the  $\Lambda$ -hyperons remain nevertheless the most abundant non-nucleonic species. Their lower mass compared with those of  $\Sigma^-$ - and  $\Xi^-$ -hyperons and more attractive potential in nuclear matter compensate the effect of the charge chemical potential.

In the case of  $NY\Delta$  matter,  $\Delta^-$  is the first heavy baryon to appear. Its onset strongly affects the hyperonic abundances: the threshold densities for the appearance of  $\Lambda$  and

<sup>2</sup> <https://compose.obspm.fr/>



Moreover, the heavy baryon fractions increase with temperature, and eventually, all allowed particle degrees of freedom can be populated. As visible from Fig. 2, the dependence on  $n_B$  is not always monotonic, due to the competition among different species. Still, due to the large negative charge chemical potential in matter with low charge fractions, negatively charged baryons nucleate at lower densities and are more abundant than their neutral and positive counterparts. The charge chemical potential decreases with the charge fraction, such that the effect becomes more pronounced at low values of  $Y_{L,e}$ . Thus,  $\Lambda$ -hyperons are the most abundant non-nucleonic species, except for low values of  $Y_{L,e}$ , where the  $\Delta^-$  abundance can exceed the  $\Lambda$  one. Our results qualitatively agree with the findings by Oertel et al. (2012); Oertel et al. (2016), where a large number of EoS models with hyperons was considered, and by Malfatti et al. (2019) concerning the  $\Delta$ s.

### 3.2 Equation of state

Fig. 3 shows the temperature as function of baryon number density for matter composed of nucleons (N), nucleons and hyperons (NY), and nucleons, hyperons and  $\Delta$  (NY $\Delta$ ), as predicted by the DDME2, DDME2Y, and DDME2Y $\Delta$  model, respectively. The top panel compares different values of  $S/A$  for the same  $Y_{L,e} = 0.2$  whereas the middle panel compares different values of  $Y_{L,e}$  for the same  $S/A = 1$ . For purely nucleonic matter, a strong increase of temperature with density is observed over the entire density range, whereas the increase is much less steep as soon as additional particles appear. Temperature can even decrease with the density over a certain range, see *e.g.* the curves for  $S/A = 1$  for the DDME2Y and DDME2Y $\Delta$  models. The change of slope is due to the sequential onset of heavy baryons (see Fig. 2). A comparison between the results obtained for N, NY and, respectively, NY $\Delta$  matter proves that for fixed values of ( $n_B, Y_{L,e}, S/A$ ), lower values of temperature are reached in systems with more particle degrees of freedom. This can be explained by the fact that, at a given temperature, the entropy of a system increases with the number of constituent particles. The effect was already discussed by Oertel et al. (2016), who confronted the behavior of matter composed of nucleons and hyperons to that of purely nucleonic matter and, respectively, nucleons and  $\Lambda$ -hyperons. They also showed that, for fixed  $n_B$  and  $S/A$ , the uncertainties in the modeling of the nucleonic sector, especially in the isovector channel, induce larger variations in temperature than those arising from modeling hyperonic matter, see the results corresponding to the purely nucleonic EoS of Lattimer & Swesty (1991), labelled “LS220”, the IUFSU (Fattoyev et al. 2010) version of Fischer et al. (2014) labelled “HS(IUF)” as well as the hyperonic EoS “SFHoY” (Fortin et al. 2018) at  $S/A = 2$  and  $Y_{L,e} = 0.2^4$ , plotted in the bottom panel.

The middle panel of Fig. 3 demonstrates that, for given baryon content of matter (*i.e.* N vs. NY vs. NY $\Delta$ ) and fixed values of  $S/A$  and  $n_B$ , the temperature depends on  $Y_{L,e}$ . In all cases, for a given  $S/A$ , the temperature decreases with increasing  $Y_{L,e}$ . The amplitude of this effect depends

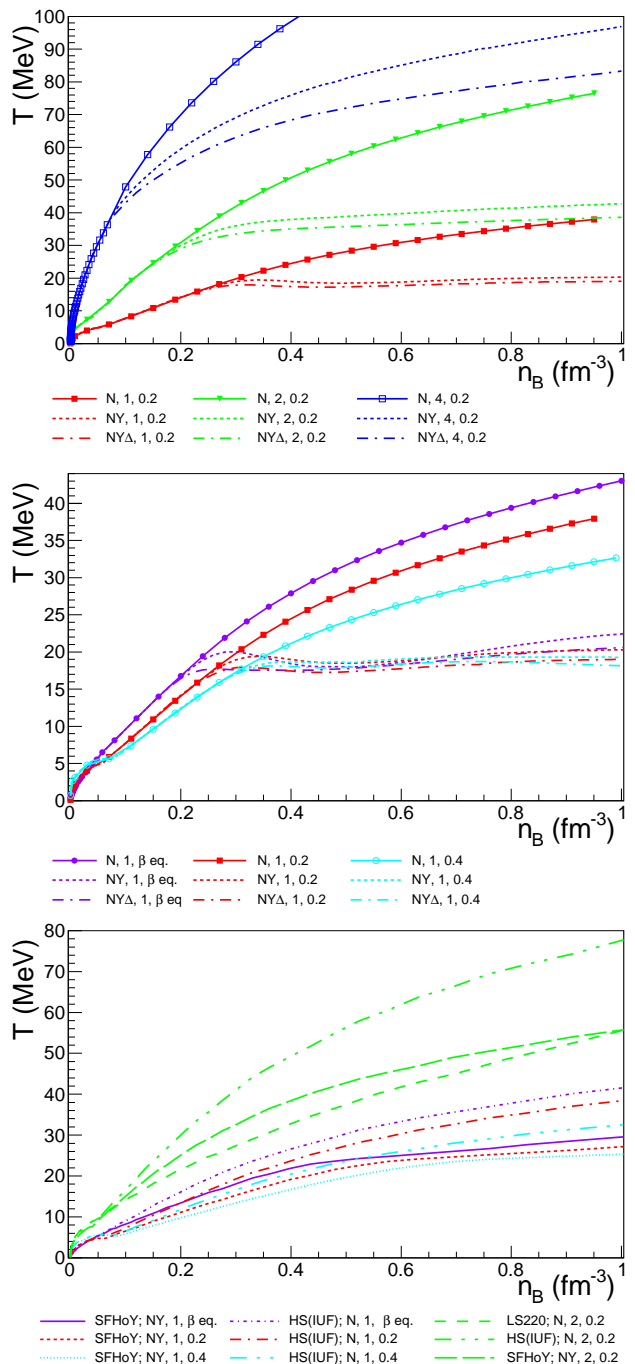


**Figure 3.** Temperature versus baryon number density for hot star matter whose baryonic sector allows for nucleons (N), NY and NY $\Delta$ . Top panel: predictions of DDME2(Y $\Delta$ ) model for different values of  $S/A$  and  $Y_{L,e} = 0.2$ , as given in the legend in the format  $S/A, Y_{L,e}$ . Middle panel: the same for  $S/A = 1$  and varying  $Y_{L,e}$  as well as  $\mu_{L,e} = 0$ . Bottom panel: predictions of purely nucleonic EoS models LS220 (Lattimer & Swesty 1991) and HS(IUF) (Fischer et al. 2014) as well as hyperonic SFHoY EoS (Fortin et al. 2018), for different values of  $S/A, Y_{L,e}$ . In all cases  $Y_{L,\mu} = 0$ .

<sup>4</sup> These EoS are available on the Compose database.

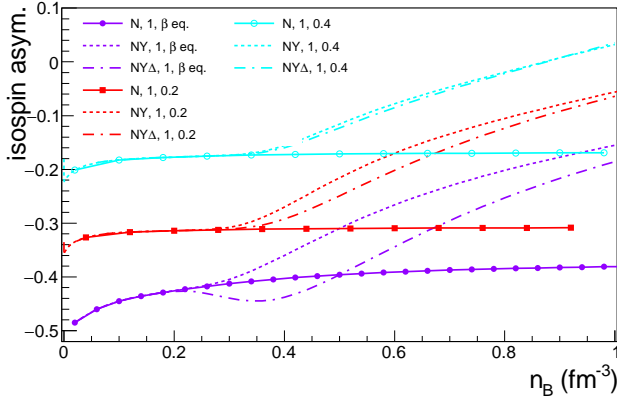


**Figure 4.** Isospin asymmetry  $\sum_i t_{3,i} n_i$  as a function of particle number density for  $\beta$ -equilibrated, neutrino-transparent, matter and matter with constant (electron) lepton fractions at  $S/A = 1$ , as predicted by DDME2, DDME2Y and DDME2Y $\Delta$  models.

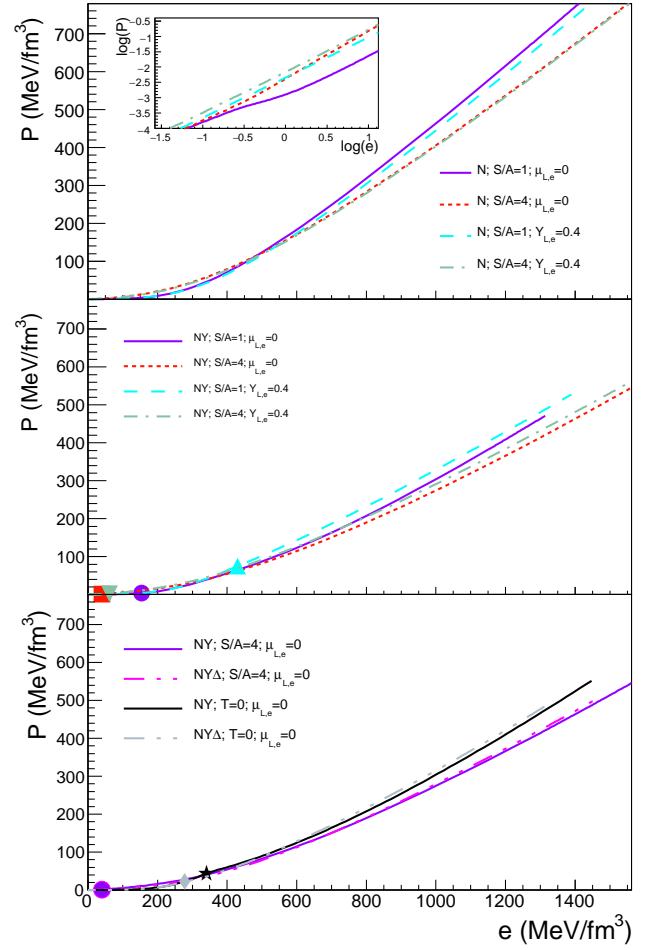
on the available particle degrees of freedom via the overall isospin asymmetry of matter, shown in Fig. 4. The smaller this asymmetry, the smaller the temperature variation as a function of  $Y_{L,e}$ . In particular, in the presence of hyperons, isospin asymmetry becomes reduced for a given  $Y_{L,e}$ , reflecting the fact that some neutrons are replaced by  $\Lambda$ -hyperons, such that the temperature variation is weaker.

Fig. 5 shows the dependence of total pressure on the total energy density. Predictions for purely nucleonic matter (top) are confronted with those corresponding to matter composed of nucleons and hyperons (middle panel) for  $S/A = 1$  and 4, at  $\mu_{L,e} = 0$  and  $Y_{L,e} = 0.4$ . The lower panel shows the impact of the onset of  $\Delta$ s at  $\mu_{L,e} = 0$  and  $S/A = 0$  and 4. We find that i) for low energy densities  $e \lesssim 300$  MeV/fm<sup>3</sup>, the pressure increases with  $(S/A)$ , whereas the opposite is true at higher energy densities; ii) the dependence of the pressure on  $Y_{L,e}$  is complex; for purely nucleonic matter at high  $e$ , pressure is higher for lower  $Y_{L,e}$ -values, whereas the opposite is observed for matter containing hyperons; for intermediate energy-densities lower  $Y_{L,e}$ -values lead to lower values of pressure, no difference between nucleonic and hyperonic EoS are observed here since hyperons have not yet nucleated; iv) the nucleation of  $\Delta$ s softens  $P(e)$  over intermediate energy-densities and stiffens it for high  $e$ ; the magnitude of the modification increases with  $\Delta$  abundances and, thus, with  $(S/A)$ . These results are in agreement with (Li et al. 2018), who discussed in detail the effect of  $\Delta$ s on the EoS of cold  $\beta$ -equilibrated matter.

### 3.3 Global properties of hot compact stars

Now we turn to the discussion of global properties of hot compact stars using as input the EoS models presented in the previous sections. Before discussing our detailed findings for hot stars, let us recall some general relations observed in older,  $\beta$ -equilibrated stars.

- The maximum mass of a compact star is sensitive to the interactions in the high-density domain and serves as a useful diagnostics of the composition of matter, in particular, nucleation of heavy baryons and/or quark



**Figure 5.** EoS for different values of  $S/A$  and  $Y_{L,e}$  (or  $\mu_{L,e} = 0$ ), as given in the legend according to the DDME2(Y $\Delta$ ). The inset in the top panel illustrates the behavior of the nucleonic matter EoS in the intermediate energy density range. The modifications of the EoS due to the onset of  $\Delta$ s are illustrated in the bottom panel for the case of  $\beta$ -equilibrated, neutrino-transparent matter. The onset of heavy baryons is marked, in each case, by a symbol.

matter (Weissenborn et al. 2012a,b; Bonanno & Sedrakian 2012; Colucci & Sedrakian 2013; Miyatsu et al. 2013; van Dalen et al. 2014; Gusakov et al. 2014; Oertel et al. 2015; Fortin et al. 2016, 2017),

- The radius of a canonical mass  $M_G \simeq 1.44M_\odot$  compact star significantly constrain the intermediate-density domain, where the value of the symmetry energy and its slope play an important role (Steiner et al. 2010; Lattimer & Steiner 2014).

- The tidal deformabilities of compact stars are strongly correlated with the radius of the star (Postnikov et al. 2010) and put constraint(s) on the intermediate-density range of the EoS (Raaijmakers et al. 2019). Their measurement in the GW170817 event (Abbott et al. 2017) has already ruled out stiff EoS (Most et al. 2018; Paschalidis et al. 2018).

- The compact star moment of inertia depends sensitively to the EoS in the intermediate- to low-density regime (Ravenhall & Pethick 1994; Lattimer & Prakash

2001; Bejger et al. 2005; Lattimer & Schutz 2005). The difference between the moments of inertia of hypernuclear and nucleonic stars and the amount of strangeness supported by the hypernuclear star are strongly correlated (Fortin et al. 2020).

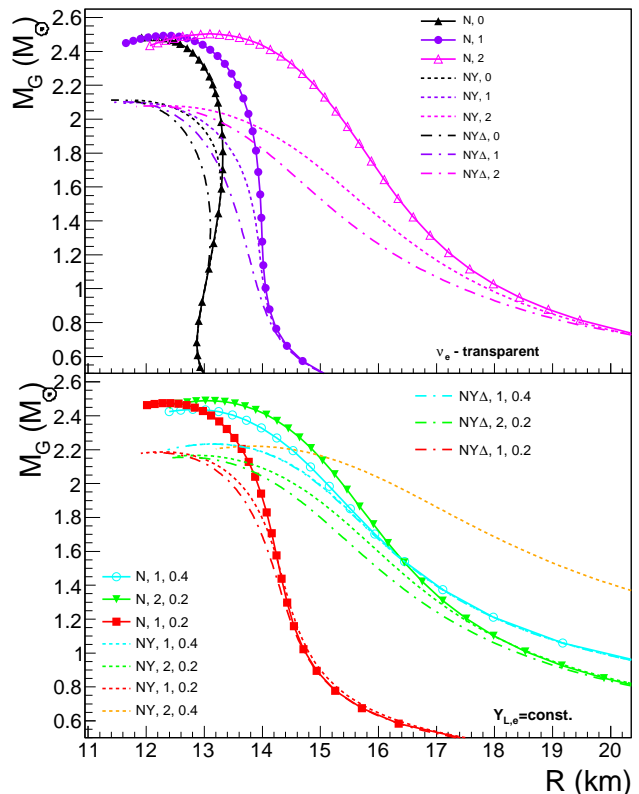
- The thermal evolution of compact stars is a sensitive probe of their interior physics and depends on the EoS mostly via the composition of matter in the dense interiors and occurrence of various direct Urca processes at high densities. Other uncertainties include the composition of the atmosphere and pairing gaps of various baryonic species that experience attractive interactions (Sedrakian & Clark 2019). Conservative models based on “minimal cooling paradigm” which assume nucleonic stars and absence of dUrca processes are so far consistent with the data (Page et al. 2004, 2009). Recent studies of the thermal evolution of hypernuclear compact stars with modern EoS (Raduta et al. 2018, 2019; Negreiros et al. 2018; Grigorian et al. 2018) show that agreement with the data can be achieved in this case as well due to a combination of accelerated cooling via various dUrca processes and suppression of their rates by superfluidity of heavy baryons. Still, any evidence for accelerated cooling cannot be attributed to heavy baryonic cores of compact stars, as models which feature nucleonic dUrca (see *e.g.* Beznogov & Yakovlev (2015); Wei et al. (2019)) or quark matter (Hess & Sedrakian 2011; de Carvalho et al. 2015; Sedrakian 2016a; Wei et al. 2020) in the centers of compact stars predict accelerated cooling as well. An accelerated cooling can also result from the emission of particles beyond the standard model, such as QCD axions or axion-like particles (Sedrakian 2016b, 2019; Beznogov et al. 2018; Leinson 2019).

Fig. 6 illustrates the dependence of the star’s gravitational mass on the circumferential radius.  $\beta$ -equilibrated stars and stars with constant electron lepton fraction are considered for different values of entropy per baryon. The results for baryonic matter composed of  $N$ ,  $NY$ ,  $NY\Delta$  are compared assuming  $Y_{L,\mu} = 0$ .

Let us start the discussion with the results at zero temperature, depicted in the top panel of Fig. 6. Naturally, the population of additional degrees of freedom such as hyperons or  $\Delta$ s modifies both compact star masses and radii. Nucleation of hyperons entails a significant reduction of the maximum mass; if in addition  $\Delta$ s are accounted for, the maximum mass is only slightly modified; see Table 2, too.

Both the population of hyperons and  $\Delta$ s reduce the star’s radius. Since the critical density for the onset of  $\Delta$ s is lower than that for hyperons, the effect on the radius is visible for the DDME2 $Y\Delta$  parameterisation at lower masses than for the DDME2Y parameterisation, see Table 2 for the respective onset masses. Since for a canonical mass star  $1.44M_{\odot}$ , hyperons are present only in a very small amount, the impact on the radius is small, whereas, within DDME2 $Y\Delta$ , the reduction is noticeable (0.16 km), see Table 2. This finding is in agreement with the results by Spinella (2017); Li et al. (2018); Li et al. (2020); Li & Sedrakian (2019b); Ribes et al. (2019), where different underlying nucleonic EoS models have been employed.

Let us now turn to the case of hot compact stars. Top and bottom panels respectively depict results corresponding to  $\beta$ -equilibrated stars and stars with constant (electron)



**Figure 6.** Gravitational mass  $M_G$  versus radius for non-rotating spherically-symmetric stars for the DDME2( $Y\Delta$ ) EoS models. Top panel:  $\beta$ -equilibrated, neutrino-transparent stars for different values of  $S/A$ . Bottom panel: Stars with constant electron lepton fraction for different values of  $S/A$  as indicated in the legend in the format  $S/A, Y_{L,e}$ .

lepton fraction. A word of caution is necessary here which concerns, in particular, the shown radii. For cold compact stars it is well known that radii are sensitive to the crust EoS and the matching of core and crust (Fortin et al. 2016). Good experimental constraints on the compact star outer crust composed of stable nuclei combined with a thermodynamically consistent treatment employing the same interaction over the whole density range, limit these uncertainties to  $\approx 5\%$  (Fortin et al. 2016). Finite-temperature EoS are expected to be affected by consistency issues related to the transition to a clustered matter close to the surface, too. An additional problem arises since in general the tabulated finite-temperature EoS contain entries for  $T \geq 0.1$  MeV. For the EoS studied in this work, the lowest density at which a solution for the desired  $S/A$  can be found in the tables lies in the range  $n_{ll} \approx 10^{-8} - 10^{-7} \text{ fm}^{-3}$ , the exact values depending on the EoS and the  $S/A$  and  $Y_{L,e}$  values. To define the surface in a coherent way for all models and  $(S/A, Y_{L,e})$  conditions, we choose a common  $n_{min} \approx 10^{-15} \text{ fm}^{-3}$  and extrapolate all EoS for  $n_{min} \leq n_B < n_{ll}$  with linear dependencies  $\log(n_B) - \log(e)$  and, respectively,  $\log(n_B) - \log(P)$ . This extrapolation together with the arbitrarily chosen transition density  $n_t = n_s/2$  between the homogeneous and inhomogeneous matter lead to some uncertainties in compact star radii and radius-dependent quantities, *e.g.* compactness

Model	$M_{B,\max}/M_{\odot}$	$Y_{L,e}$	instab. domain	$Y_{L,e}$	instab. domain	$Y_{L,e}$	instab. domain
HS(IUF)	2.26	0.4	$S/A \geq 3.28$	0.2	$S/A \geq 2.13$		
LS 220	2.40					0.1	$S/A \leq 1.57$
SFHo	2.45						
SFHoY	2.36						
DDME2	3.02						
DDME2Y	2.48	0.4	$S/A \leq 1.82$	0.2	$S/A \leq 1.67$	0.1	$S/A \leq 1.16$
DDME2Y $\Delta$	2.49	0.4	$S/A \leq 1.64$	0.2	$S/A \leq 1.60$	0.1	$S/A \leq 1.19$

**Table 3.** Maximum baryonic masses of cold catalyzed neutrino-transparent compact stars based on different EoS models and domains of instability with respect to collapse to BH (Bombaci 1996), for  $Y_{L,e} = 0.1, 0.2, 0.4$ .

$C = M_G/R$ , the moment of inertia, quadrupole moment and tidal deformability. Masses are not affected. For  $S/A \lesssim 2$  the uncertainties on the radii are smaller than a few percents and those on other quantities even smaller, see Appendix. As such this somewhat arbitrary treatment of the compact star surface affects neither the properties of hot stars discussed in this section nor the conclusions of Sections 4.1 and 4.2, where universal relations between different compact star properties are addressed.

The dependence of the maximum gravitational mass  $M_{G,\max}$  on the star’s entropy per baryon is shown in Fig. 7. Note that the maximum masses in Fig. 7 have been determined at constant total entropy  $(S/A)M_B$ , where  $M_B$  denotes the star’s baryonic mass following the turning point criterion for a configuration to be secularly stable; see (Sorkin 1982; Goussard et al. 1998; Marques et al. 2017) for a detailed discussion. The following features are observed in Figs. 6 and 7:

i) for purely nucleonic stars thermal effects increase the gravitational mass and, thus,  $M_{G,\max}$ , whereas stars with an admixture of heavy baryons manifest a non-monotonic dependence of  $M_{G,\max}$  on  $S/A$ . The reason is that as long as thermal effects favor nucleation of new species, the maximum mass decreases with  $S/A$ ; as soon as all available degrees of freedom are populated, we recover the behavior observed for purely nucleonic stars, *i.e.*  $M_{G,\max}$  increases with  $S/A$ .

ii) for purely nucleonic stars at fixed  $S/A$   $M_{G,\max}(\mu_{L,e} = 0) > M_{G,\max}(Y_{L,e} = 0.2) > M_{G,\max}(Y_{L,e} = 0.4)$  with the exception of LS220 at  $S/A > 3.5$ . Compact stars with an admixture of heavy baryons most frequently show the opposite effect, *i.e.*  $M_{G,\max}$  increases with  $Y_{L,e}$ ; the reason lies in fact that a lepton rich environment with large  $Y_{L,e}$  disfavors heavy baryons, such that they become less populated and the maximum mass can thus increase with  $Y_{L,e}$  for given  $S/A$ ; out of the considered cases the only exception to this rule is the case of SFHoY EoS with  $S/A \leq 1$  for which  $M_{G,\max}(Y_{L,e} = 0.4) < M_{G,\max}(Y_{L,e} = 0.2)$ .

iii) higher values of  $Y_{L,e}$  reduce the star’s compactness, see Fig. 6;

iv) for a given mass and composition, radii increase with  $S/A$ , *i.e.* thermal effects reduce the star’s compactness, see Fig. 6;

v) the magnitude of thermal effects depends on the EoS; for DDME2 thermal effects are smaller than those due to  $Y_{L,e}$  and the number of allowed degrees of freedom; for LS220 thermal effects dominate over those related to  $Y_{L,e}$ .

vi) nucleation of  $\Delta$ s reduces the gravitational mass, including  $M_{G,\max}$ . Since the effect scales with  $\Delta$  abundance, it increases with  $S/A$  and decreases with  $Y_{L,e}$ .

The maximum gravitational mass of isentropic compact stars in  $\beta$ -equilibrium is relevant for BH formation in a failed CCSN. By performing many simulations, Schneider et al. (2020) have recently shown that BH formation occurs soon after the PNS’s gravitational mass overcomes  $M_{G,\max}$  corresponding to its most common entropy value. The trajectory is thereby essentially determined by the progenitor compactness, such that the EoS dependence enters mainly via the behavior of  $M_{G,\max}$  as function of  $S/A$ .

The maximum baryon mass is an interesting quantity in the context of stability against collapse to a black hole during PNS and BNS merger evolution. In the absence of accretion,  $M_B$  is a conserved quantity during evolution, such that if it exceeds the maximum baryon mass of the cold  $\beta$ -equilibrated configuration, the star necessarily becomes unstable against collapse to a black hole at some point independently of the mechanism stabilising it temporarily, be it strong differential rotation (Baumgarte et al. 2000; Morrison et al. 2004; Kastaun & Galeazzi 2015), the lepton rich environment in PNS (Prakash et al. 1997) or thermal effects (Prakash et al. 1997; Kaplan et al. 2014). Following this reasoning, Bombaci (1996); Prakash et al. (1997) conjectured that thermally populated non-nucleonic degrees of freedom lead to the existence of meta-stable objects, *i.e.* stars which during the PNS evolution have a larger maximum baryonic mass than their cold,  $\beta$ -equilibrated counterparts and which upon deleptonization and cooling necessarily collapse to a black hole.

Our results for the maximum baryonic mass, shown as a function of entropy per baryon  $S/A$  for constant (electron) lepton fractions are plotted in Fig. 8 together with results corresponding to LS220, HS(IUF), SFHoY and SFHo (Steiner et al. 2013) EoS models. The chosen values of the (electron) lepton fraction,  $Y_{L,e} = 0.1$  (bottom), 0.2 (middle) and 0.4 (top panel), are relevant for the Kelvin-Helmholtz epoch (Pons et al. 1999). Again, the maximum mass has been determined at a fixed total entropy  $(S/A)M_B$ , see Goussard et al. (1998); Marques et al. (2017). Table 3 gives, for all models, the values of  $M_{B,\max}(0, \mu_{L,e} = 0)$ ; also we give, for the considered  $Y_{L,e}$  values, the instability domains defined according to Bombaci (1996). The values of  $S/A$  where  $M_{B,\max}(S/A, Y_{L,e}) = M_{B,\max}(0, \mu_{L,e} = 0)$  are marked with symbols in Fig. 8. DDME2Y( $\Delta$ ) models show an instability for relatively low  $S/A$ , whereas the nucleonic version DDME2 stays stable over the entire range of considered values for  $S/A$ . In simulations, during the Kelvin-Helmholtz phase,  $S/A$  stays around 1-2, such that within DDME2 the population of hyperons and/or  $\Delta$  might indeed lead to the formation of a meta-stable object. However, this does not seem to be possible exclusively

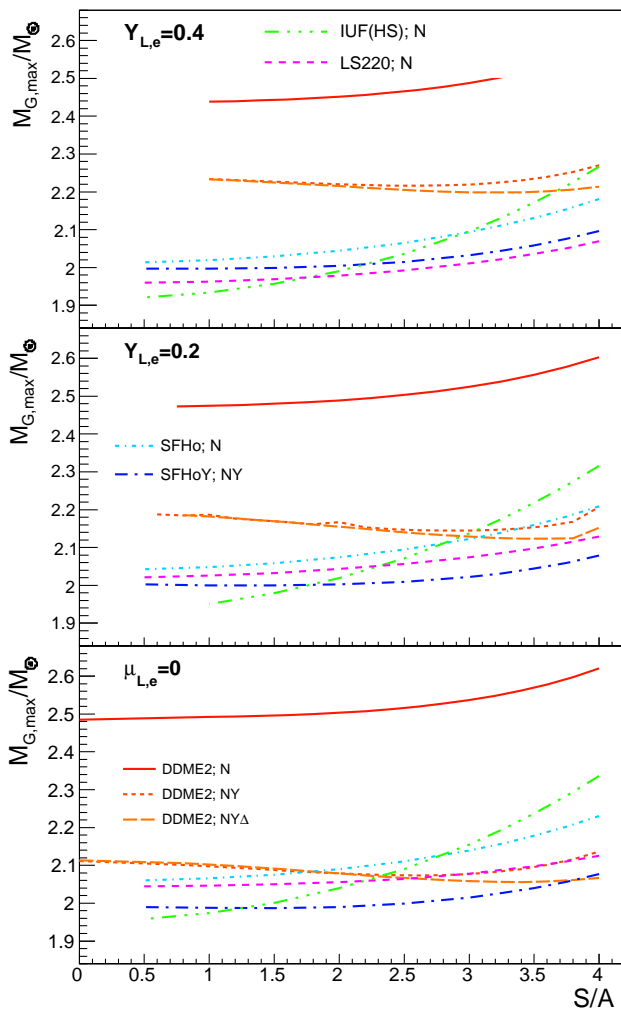


**Figure 7.** Maximum gravitational mass  $M_{G,\max}$  versus entropy per baryon  $S/A$  for non-rotating spherically-symmetric compact stars based on the DDME2( $Y\Delta$ ), HS(IUF) (Fischer et al. 2014), LS220 (Lattimer & Swesty 1991), SFHo (Steiner et al. 2013) and SFHoY (Fortin et al. 2018) models for  $\mu_{L,e} = 0$  (bottom) as well as  $Y_{L,e} = 0.2$  (middle) and  $0.4$  (top panel). Results for purely nucleonic stars and stars with admixtures of heavy baryons are considered.

in models with non-nucleonic degrees of freedom. The purely nucleonic HS(IUF) and LS220 show instabilities too. Although it is not clear whether they will be experienced in the stellar evolution without performing simulations, it cannot be excluded that meta-stable nucleonic stars could form. These results show the importance of the nuclear interaction in understanding the properties of the high-density EoS.

#### 4 UNIVERSAL RELATIONS

Although NS properties depend sensitively on the EoS, several “universal” relations have been found between global quantities. The term “universality” refers here to very weak dependence on the EoS which holds well for cold  $\beta$ -equilibrated stars. Although so far the reason for this universal behavior is not well understood, it may be exploited to

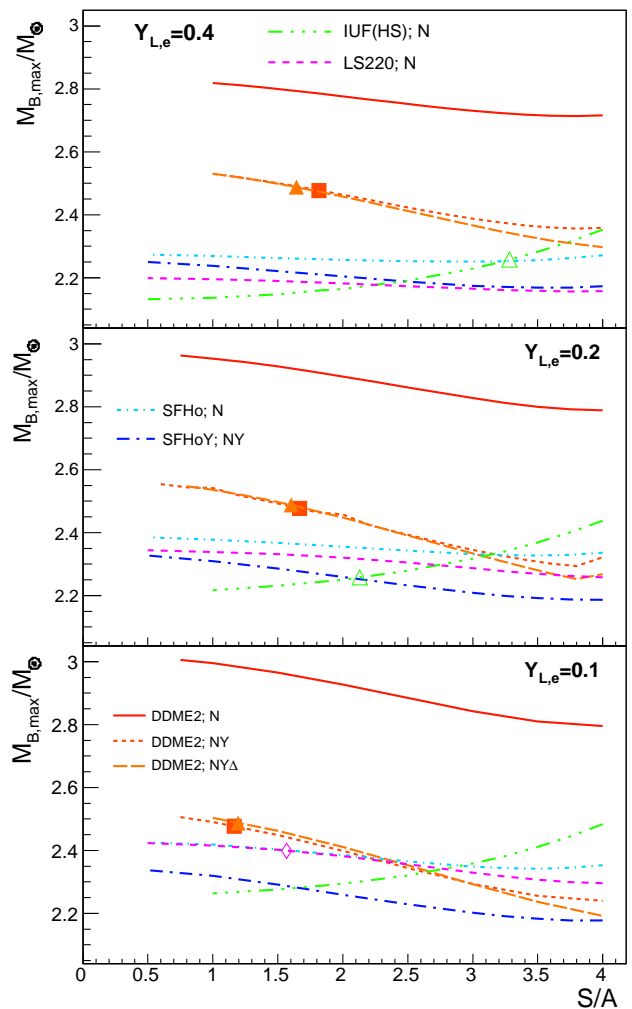


**Figure 8.** Maximum baryonic mass  $M_{B,\max}$  versus entropy per baryon  $S/A$  for non-rotating spherically-symmetric compact stars based on the DDME2( $Y\Delta$ ), HS(IUF) (Fischer et al. 2014), LS220 (Lattimer & Swesty 1991), SFHo (Steiner et al. 2013) and SFHoY (Fortin et al. 2018) EoS models for  $Y_{L,e} = 0.1$  (bottom),  $0.2$  (middle) and  $0.4$  (top panel). Results for purely nucleonic stars and stars with admixtures of heavy baryons are considered. The value of  $S/A$  where the maximum baryonic mass at  $Y_{L,e} = \text{const.}$  equals the maximum baryonic mass of the corresponding cold  $\beta$ -equilibrated, neutrino-transparent star is marked by solid square (DDME2(NY)), solid triangle (DDME2(NY $\Delta$ )), open triangle (IUF(HS)), and diamond (LS220).

constrain quantities difficult to access observationally, eliminate the uncertainties related to the EoS in the analysis of the data, or break degeneracies between integral quantities, (e.g., the quadrupole moment and the neutron-star spins in binary in-spiral waveforms).

In this section, we shall investigate to what extent this universality remains valid for hot and lepton rich stars, allowing for various particle degrees of freedom in the EoS. Section 4.1 will address relations between the normalised moment of inertia, quadrupole moment, tidal deformability and binding energy and the star’s compactness, and Section 4.2 will address the  $I$ -Love- $Q$  relations. Binding en-

Thermo. cond.	$p_0$	$p_1$	$p_2$	$p_3$	$p_4$	Refs.
$T = 0, \beta\text{-eq.}$ $S/A = 2, Y_{L,e} = 0.2$	$c_0$ 0.244	$c_1$ 0.638	$c_2$ 0	$c_3$ 0	$c_4$ 3.202	(Breu & Rezzolla 2016) this work
$T = 0, \beta\text{-eq.}$ $S/A = 2, Y_{L,e} = 0.2$		$a_1$ $8.134 \cdot 10^{-1}$ $9.447 \cdot 10^{-1}$	$a_2$ $2.101 \cdot 10^{-1}$ $1.815 \cdot 10^{-1}$	$a_3$ $3.175 \cdot 10^{-3}$ $-4.049 \cdot 10^{-3}$	$a_4$ $-2.717 \cdot 10^{-4}$ $4.339 \cdot 10^{-5}$	(Breu & Rezzolla 2016) this work
$T = 0, \beta\text{-eq.}$ $S/A = 2, Y_{L,e} = 0.2$		$b_1$ $3.71 \cdot 10^{-1}$ $3.632 \cdot 10^{-1}$	$b_2$ $-3.91 \cdot 10^{-2}$ $-4.216 \cdot 10^{-2}$	$b_3$ $1.056 \cdot 10^{-3}$ $1.288 \cdot 10^{-3}$		(Maselli et al. 2013) this work
$T = 0, \beta\text{-eq.}$ $S/A = 2, Y_{L,e} = 0.2$	$e_0$ -2.7157 -1.8410	$e_1$ 0.7017 0.5829	$e_2$ 0.1611 0.1081	$e_3$ $-6.4977 \cdot 10^{-3}$ $-4.3085 \cdot 10^{-3}$		this work this work
$T = 0, \beta\text{-eq.}$ $S/A = 2, Y_{L,e} = 0.2$		$d_1$ 0.6213 0.4733	$d_2$ 0.1941 0.9232			(Breu & Rezzolla 2016) this work

**Table 4.** Fitting parameters entering Eqs. (21)-(25) under different indicated thermodynamic conditions.

ergies and tidal deformabilities will be calculated for non-rotating spherically-symmetric stars; moments of inertia and quadrupole deformations will be calculated for rigidly and slowly rotating stars.

#### 4.1 Dependence on the compactness

For cold,  $\beta$ -equilibrated stars in the slow-rotation approximation, several authors have established relations between the compactness of a star  $C = M_G/R$  and normalised moment of inertia, quadrupole moment, tidal deformability and binding energy, which show universal character, *i.e.* are almost EoS independent.

First, by considering different EoS for cold  $\beta$ -equilibrated neutron star matter Ravenhall & Pethick (1994) noted that, except for very low mass stars, the normalised moment of inertia  $\tilde{I} = I/(M_G R^2)$  behaves as a universal function of the star's mass and radius,

$$\tilde{I} \approx 0.21 \frac{1}{1 - 2M_G/R}. \quad (20)$$

Later, Lattimer & Schutz (2005) proved that  $\tilde{I}$  can be expressed as a polynomial in compactness:

$$\tilde{I} = c_0 + c_1 C + c_2 C^2 + c_3 C^3 + c_4 C^4. \quad (21)$$

The issue was recently reconsidered by Breu & Rezzolla (2016) who showed that the dispersion between different EoS in Eq. (21) is reduced if only models which fulfill the  $2M_\odot$  maximum mass constraint are considered. Furthermore, they found another universal relation, relating alternatively normalised moment of inertia  $\tilde{I} = I/M_G^3$  [note the different normalisation with respect to Eq. (21)] to compactness

$$\tilde{I} = a_1 C^{-1} + a_2 C^{-2} + a_3 C^{-3} + a_4 C^{-4}. \quad (22)$$

Maselli et al. (2013) introduced a universal expression relating compactness to the normalised tidal deformability  $\bar{\lambda} = \lambda/M_G^5$

$$C = b_1 + b_2 \ln \bar{\lambda} + b_3 (\ln \bar{\lambda})^2. \quad (23)$$

Earlier, by considering a collection of different EoS models, Yagi & Yunes (2013a) have shown that the scaled quadrupole moment  $\bar{Q} = Q M_G/J^2$ , where  $J$  stands for

the angular momentum, as function of compactness is only weakly dependent on the EoS. Our results suggest that  $\bar{Q}$  can be expressed as a polynomial of  $C^{-1}$

$$\bar{Q} = e_0 + e_1 C^{-1} + e_2 C^{-2} + e_3 C^{-3}. \quad (24)$$

which is analogous to Eq (22) for  $\tilde{I}$ . The neutron star binding energy, defined as the difference between baryonic and gravitational masses  $E_B = M_B - M_G$ , shows little sensitivity on the underlying EoS model if normalised by the gravitational mass (Lattimer & Prakash 2001; Breu & Rezzolla 2016). According to Lattimer & Prakash (2001) it behaves as

$$\frac{E_B}{M_G} = \frac{d_1 C}{1 - d_2 C}. \quad (25)$$

Again, as in the case of  $\tilde{I}(C)$ , limiting the considered EoS models to those which are consistent with the  $2M_\odot$  mass constraint improves the quality of the fit (Breu & Rezzolla 2016). The values of the different fitting parameters,  $a_i$ ,  $b_i$ ,  $c_i$ ,  $d_i$ ,  $e_i$ , entering Eqs. (21)-(25) are provided in Table 4.

Let us now turn to the discussion of universality at nonzero entropy. The top panels of Figs. 9, 10, 11 and 12 illustrate, respectively, the behavior of  $\tilde{I}$ ,  $\bar{Q}$ ,  $\bar{\lambda}$ , and  $E_B/M_G$  as a function of compactness for different combinations of constant  $S/A$  and  $Y_{L,e}$ , as obtained from the DDME2( $Y\Delta$ ) model. The moment of inertia is thereby calculated to leading order in the slow, rigid rotation approximation (Hartle 1967) and the tidal deformability  $\lambda$  is computed following Hinderer (2008) and Hinderer et al. (2010). The quadrupole moment is computed for a rotation frequency of 100 Hz using the public domain code Lorene<sup>5</sup> (Gourgoulhon et al. 2016). For comparison, for cold,  $\beta$ -equilibrated matter the results obtained from the DDME2( $Y\Delta$ ) model as well as the predictions of Eqs. (21)-(25) are shown, see Table 4 for the parameter values.

For all these quantities, a significant scatter of the results for different values of  $S/A$  and  $Y_{L,e}$  is observed. The deviation from the results corresponding to cold catalyzed matter increases with  $S/A$  and/or  $Y_{L,e}$ . This indicates that universality does not hold when stars with different entropies

<sup>5</sup> <https://lorene.obspm.fr>

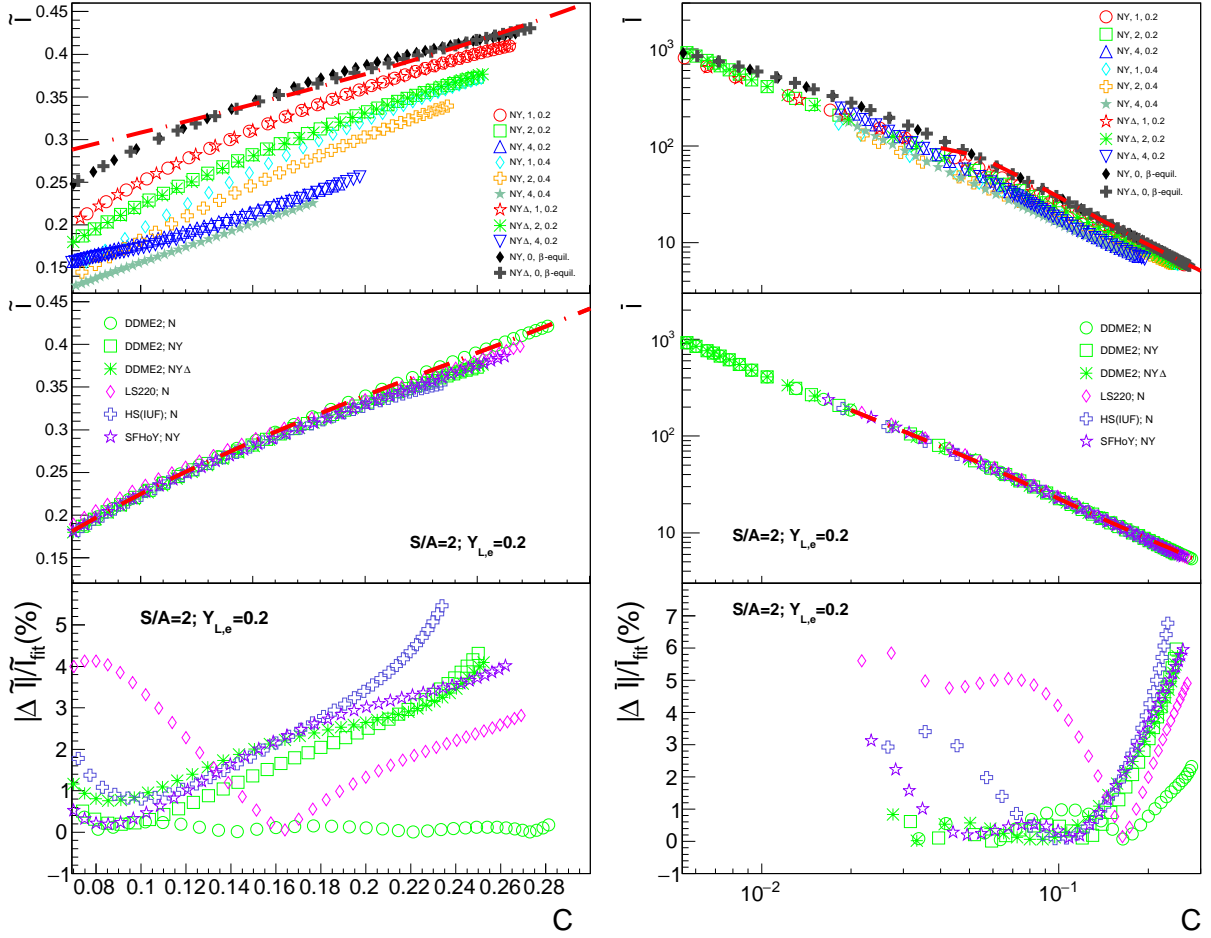


**Figure 9.** Normalised moments of inertia  $\tilde{I} = I / (M_G R^2)$  (left panels) and  $\bar{I} = I / M_G^3$  (right panels) as function of compactness  $C = M_G / R$ . Top panels: results corresponding to different thermodynamic conditions and matter compositions, as obtained from the DDME2( $Y\Delta$ ) model. At finite temperatures the thermodynamic conditions are indicated in terms of constant  $S/A$  and  $Y_{L,e}$ ; the label “0,  $\beta$ -equil.” corresponds to cold catalyzed neutrino-transparent matter. Middle panels: results corresponding to  $(S/A = 2, Y_{L,e} = 0.2)$  for different matter compositions and EoS models. The long dot-dashed curves correspond to the fits in Eqs. (21) and (22), respectively, with parameters from Table 4. Bottom panels: relative residual errors with respect to the fits in Eqs. (21) (left panel) and (22) (right panel) for the cases considered in the middle panels.

and lepton contents are compared. For  $\tilde{I}$  and  $\bar{I}$  this conclusion has recently been reached by Lenka et al. (2019). However, one needs in fact to compare quantities under identical thermodynamic conditions. To illustrate this point, we display in the middle panels of Figs. 9, 10 and 12 and bottom panel of Fig. 11 the results for different EoS models and compositions, for the case  $(S/A = 2, Y_{L,e} = 0.2)$ . In addition to matter made of  $N$ ,  $NY$  or  $NY\Delta$  based on the DDME2( $Y\Delta$ ) models, we show results corresponding to the purely nucleonic LS220 and HS(IUF) EoS models (Lattimer & Swesty 1991; Fischer et al. 2014) as well as the hyperonic SFHoY EoS (Fortin et al. 2018). The agreement between the different EoS models is very good, except for  $\tilde{I}$ ,  $\bar{Q}$ , and  $E_B$  at large values of  $C \gtrsim 0.2$ , where some deviations can be seen. This confirms that indeed universality holds well for all these relations if the same thermodynamic conditions are considered.

To quantify this universality, we have performed fits to

the nucleonic DDME2 results following Eqs. (21)–(25), indicated in the figures by the green open circles. The corresponding parameter values are listed in Table 4. Overall, the good description of the results indicates that the functional relations proposed for cold  $\beta$ -equilibrated matter hold for hot matter with trapped neutrinos, too. Only for  $\tilde{I}(C)$ , the data are better described by a third-order polynomial, see Table 4. For  $\tilde{I}(C)$ ,  $\bar{I}(C)$ ,  $\bar{Q}$  and  $C(\bar{\lambda})$  the deviations from the fits are of the order of a few percents, as illustrated in the bottom panels of Figs. 9 and 10 and, respectively, the inset in the bottom panel of Fig. 11, where the relative residual errors with respect to the fit functions are depicted. We conclude that for these quantities universality holds with a precision only slightly inferior to that for the cold  $\beta$ -equilibrated case. For  $E_B/M_G(C)$  the deviations from the fit are larger, up to 20%, see the bottom panel of Fig. 12.

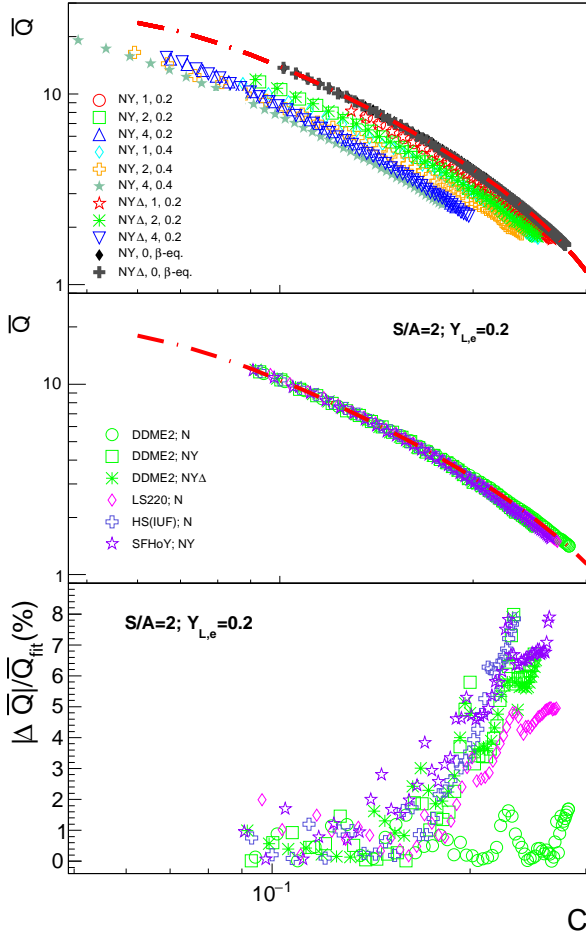


**Figure 10.** Normalised quadrupole moment  $\bar{Q}$  of slowly and rigidly rotating stars as function of compactness,  $C$ . Top panel: results corresponding to different thermodynamic conditions (mentioned in the legend) and matter compositions derived from the DDME2( $Y\Delta$ ) model. At finite temperatures the thermodynamic conditions are specified in terms of constant  $S/A$  and  $Y_{L,e}$ ; the label “0,  $\beta$ -equil.” corresponds to cold catalyzed neutrino-transparent matter. Middle panel: results corresponding to  $(S/A = 2, Y_{L,e} = 0.2)$  for different EoS models and for different matter compositions. The red dot-dashed curves correspond to fits in Eq. (24) with parameters values from Table 4. Bottom panel: relative residual errors with respect to the fit in Eq. (24) for the cases considered in the middle panels.

#### 4.2 $I$ -Love- $Q$ universal relations

Yagi & Yunes (2013b,a) identified universal relations among the pairs of quantities  $\bar{I} - \bar{Q}$ ,  $\bar{I} - \bar{\lambda}$  and  $\bar{Q} - \bar{\lambda}$ . Numerically, these relations can be cast in a polynomial form on a log-log scale,

$$\ln Y_i = a_i + b_i \ln X_i + c_i (\ln X_i)^2 + d_i (\ln X_i)^3 + e_i (\ln X_i)^4, \quad (26)$$

with the pairs  $(Y_i, X_i)$  corresponding to  $(\bar{I}, \bar{\lambda})$ ;  $(\bar{I}, \bar{Q})$ ;  $(\bar{Q}, \bar{\lambda})$ . Originally established in the slow rotation limit, these relations remain EoS independent for fast rotating stars with rotation frequency dependent fit parameters (Doneva et al. 2013).

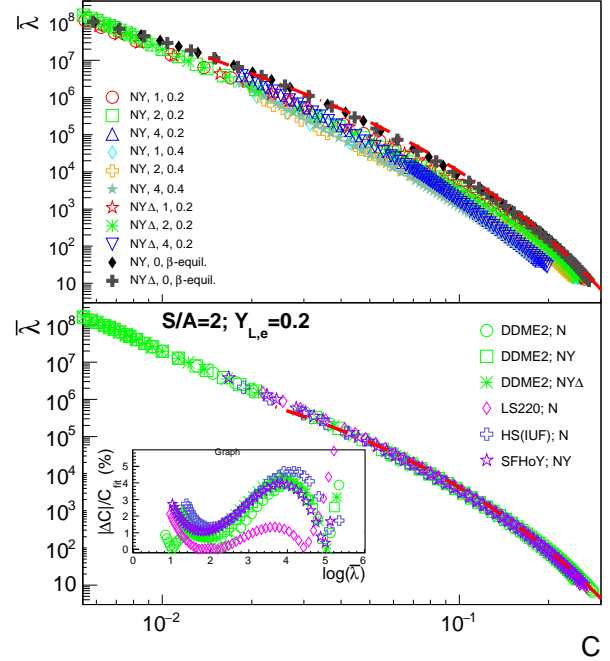


**Figure 11.** Normalised tidal deformability  $\bar{\lambda}$  of non-rotating spherically-symmetric stars as function of compactness  $C$ . Top panels: results corresponding to different thermodynamic conditions (mentioned in the legend) and matter compositions, as obtained from the DDME2( $Y\Delta$ ) model. At finite temperatures the thermodynamic conditions are specified in terms of constant  $S/A$  and  $Y_{L,e}$ ; the label “0,  $\beta$ -equil.” corresponds to cold catalyzed neutrino-transparent matter. Bottom panels: results corresponding to  $(S/A = 2, Y_{L,e} = 0.2)$  for different EoS models for different matter compositions. The red dot-dashed curves correspond to fit in Eq. (23) with parameters values from Table 4. Relative residual errors with respect to the fit in Eq. (23) are shown in the inset.

Let us now consider  $I$ -Love- $Q$  universality at nonzero temperature. We will focus here on  $\bar{I} - \bar{\lambda}$  and  $\bar{I} - \bar{Q}$ . If universality holds for these two pairs of quantities, it is very likely that it will hold for the third pair as well. In Fig. 13 we plot  $\bar{I}$  as function of  $\bar{\lambda}$  (left) and  $\bar{Q}$  (right). Again, in the top panels, we compare results for different values of  $S/A$  and  $Y_{L,e}$  employing the DDME2( $Y\Delta$ ) models with those for cold  $\beta$ -equilibrated stars. The dot-dashed line indicates the result of Eq. (26) with fitting parameters obtained for cold  $\beta$ -equilibrated stars according to the DDME2Y model, see Table 5. As can be seen from the middle panels, the residual errors become an order of magnitude larger than those obtained when considering only cold  $\beta$ -equilibrated stars (Yagi & Yunes 2013a). This deviation of the  $I$ -Love- $Q$ -relations from universality due to thermal effects have already been noted by Martinon et al. (2014); Marques et al. (2017).

The discussion in Sec. 4.1 suggests that universality at nonzero entropy can be recovered under identical thermodynamic conditions. The bottom panels of Fig. 13 show the relative error of the results with respect to Eq. (26) with refitted parameters at  $S/A = 2$  and  $Y_{L,e} = 0.2$ , see Table 5. Results corresponding to DDME2( $Y\Delta$ ) model are confronted with those of LS220 (Lattimer & Swesty 1991), HS(IUF)

$Y$	$X$	Thermo. cond.	$a$	$b$	$c$	$d$	$e$	Refs.
$\bar{I}$	$\lambda$	$T = 0, \beta$ -eq.	1.47	$7.19 \times 10^{-2}$	$2.00 \times 10^{-2}$	$-5.00 \times 10^{-4}$	$2.39 \times 10^{-6}$	this work
$\bar{I}$	$\bar{Q}$	$T = 0, \beta$ -eq.	1.50	$4.66 \times 10^{-1}$	$6.11 \times 10^{-2}$	$1.30 \times 10^{-2}$	$1.20 \times 10^{-3}$	this work
$\bar{I}$	$\bar{\lambda}$	$S/A = 2, Y_{L,e} = 0.2$	1.49	$6.55 \times 10^{-2}$	$2.06 \times 10^{-2}$	$-4.47 \times 10^{-4}$	$-2.96 \times 10^{-6}$	this work
$\bar{I}$	$\bar{Q}$	$S/A = 2, Y_{L,e} = 0.2$	1.53	$3.81 \times 10^{-1}$	$1.36 \times 10^{-1}$	$-1.21 \times 10^{-2}$	$3.45 \times 10^{-3}$	this work

Table 5. Fitting parameters of eq. (26) for different thermodynamic conditions.

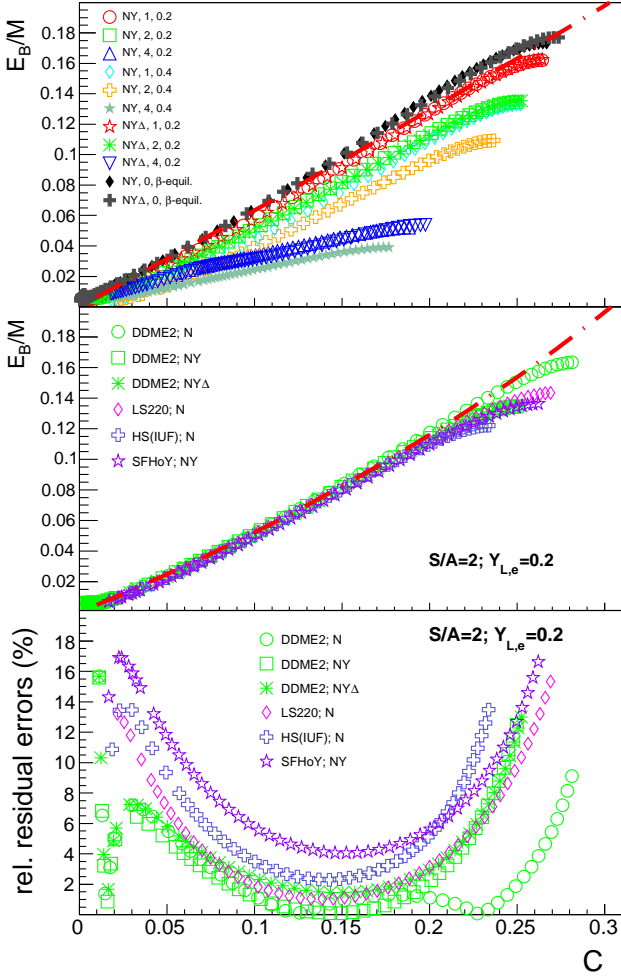
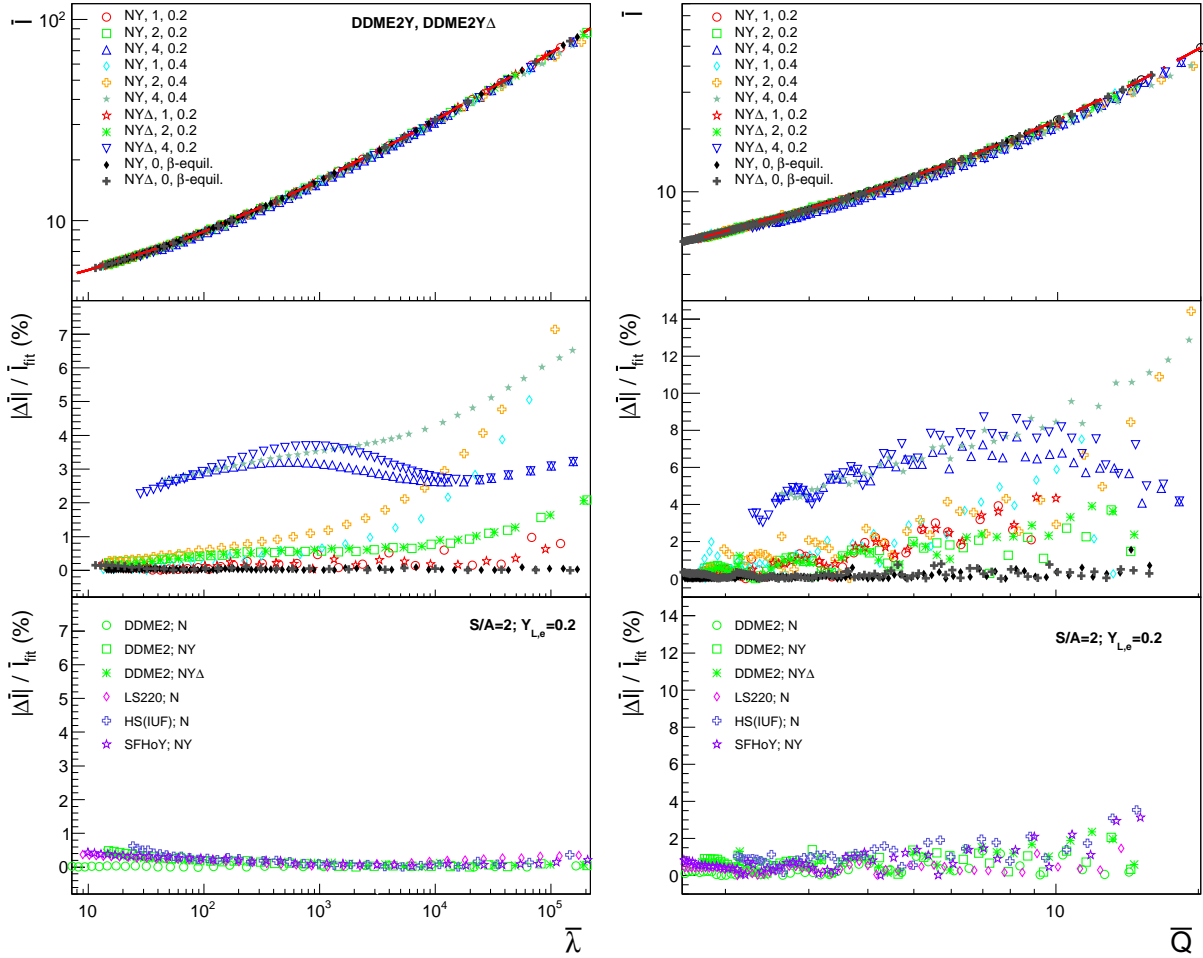


Figure 12. Binding energy per unit of gravitational mass  $E_B/M_G$  of non-rotating spherically-symmetric stars as a function of compactness  $C$ . Top panel: results corresponding to different thermodynamic conditions (indicated in the legend) and matter compositions, as obtained from the DDME2( $Y\Delta$ ) model. At finite temperatures the thermodynamic conditions are specified in terms of constant  $S/A$  and  $Y_{L,e}$ ; the label “0,  $\beta$ -equil.” corresponds to cold catalyzed neutrino-transparent matter. Middle panel: results corresponding to ( $S/A = 2, Y_{L,e} = 0.2$ ) for different EoS models and for different matter compositions. The red dot-dashed curves correspond to fits in Eq. (25) with parameters values from Table 4. Bottom panel: relative residual errors with respect to the fit for the cases considered in the middle panel.

(Fischer et al. 2014) and SFHoY (Fortin et al. 2018). The quality of the fit by Eq. (26) is considerably improved reaching the accuracy of zero temperature,  $\beta$ -equilibrated case. Thus, universality again holds under the same thermodynamic conditions.

This phenomenologically observed universality is not yet understood. Analytical solutions in the Newtonian limit (Yagi & Yunes 2013a) as well as those obtained using an expansion around this limit (Jiang & Yagi 2020) corroborate the EoS independence, but without providing a definitive insight into their origin. Yagi & Yunes (2013a) advanced two possible explanations. First, these dimensionless quantities mainly depend on the outermost shells of the core and on the crust, where, by construction, “realistic” EoS, *i.e.* nuclear EoS with parameters fitted to nuclear data and/or astrophysical observations, agree with each other. As in (Yagi & Yunes 2013a) the term “realistic” is meant here to distinguish nuclear EoS from polytropic EoS. If this was the case, finite-temperature EoS should necessarily violate universality as their low-density behaviors differ from each other, and from that of cold  $\beta$ -equilibrated matter, see the discussion in Sec. 3. Second, Yagi & Yunes (2013a) suggested that this universality could be a reminiscence of no-hair theorems as the neutron star’s compactness approaches the black hole limit. In this case, too, since hot stars are less compact, see Sec. 3, universality should be less well satisfied for hot stars.

Yagi & Yunes (2013a) corroborated their guess about the origin of universality by investigating the radial dependence of the integrands entering the calculation of moment of inertia, quadrupole moment and tidal deformability in the Newtonian limit, normalised by their values at the star’s center, showing that they are peaked around  $0.7 \lesssim r/R \lesssim 0.9$ , where  $r$  is the radial distance from the star’s center. The main contribution to these quantities thus indeed comes from the outer core and crust. In Fig. 14 we show for stars with compactness  $C = 0.17$  the radial profiles of the quantities  $(er^4/e_c R^4)$  and  $[ep_c(de/dp)/e_c^2]$ , where  $(er^4)$  corresponds to the integrand of the moment of inertia and quadrupole moment in the Newtonian limit (top panel), and  $(ede/dr)$  to the EoS-dependent contribution to the tidal deformability in the Newtonian limit (bottom panel); here index  $c$  indicates corresponding values at the star’s center. Comparing results for different  $S/A$  and  $Y_{L,e}$  (left) we note that with increasing temperature and, slightly more pronounced, increasing  $Y_{L,e}$ , the maximum of the integrands migrate to lower  $r/R$  values and smear out. For the highest considered value  $S/A = 4$ ,  $[er^4/e_c R^4]$  manifests a wide peak centered at  $r/R \approx 0.6$ , while  $(ep_c(de/dp)/e_c^2)$  shows a plateau over  $r/R \lesssim 0.6$  followed by a shoulder-like decrease. Overall, an important dispersion is obtained among the curves corresponding to different thermodynamic conditions. This is in agreement with the breakdown of universality due to thermal effects if different thermodynamic condi-



**Figure 13.** Left:  $\bar{I}$  vs.  $\bar{\lambda}$  (top) and relative residual errors  $|\Delta\bar{I}|/\bar{I}_{fit}(\bar{\lambda})$  with respect to the fit by eq. (26) (middle, bottom). Right:  $\bar{I}$  vs.  $\bar{Q}$  (top) and relative residual errors  $|\Delta\bar{I}|/\bar{I}_{fit}(\bar{Q})$  with respect to the fit by eq. (26) (middle, bottom). Top: results for different thermodynamic conditions and matter compositions (indicated in the legend), as obtained from the DDME2( $Y\Delta$ ) model. The dot-dashed red line indicates the fit to the cold  $\beta$ -equilibrated results, see Table 5. Middle: relative error with respect to the fit at zero temperature. Bottom panels: results corresponding to  $S/A = 2$  and  $Y_{L,e} = 0.2$ . The relative error with respect to refitted values under these thermodynamic conditions, see Table 5, is shown for different matter compositions and EoS models.

tions are compared. Considering again fixed  $S/A = 2$  and  $Y_{L,e} = 0.2$  (right), the predictions of the different models agree very well over the whole star’s volume. We, therefore, conclude that the explanation for  $I$ –Love– $Q$  universality does not lie in the similar behavior of “realistic” EoS in the outer core and the crust but rather in the similar behavior of EoS over the density domains which, under the considered thermodynamic condition, play the most important role.

## 5 CONCLUSIONS

In this work, we constructed EoS of dense matter with heavy baryons (hyperons and  $\Delta$ -resonances) at non-zero temperature and for different lepton fractions within the covariant density functional theory. This extends models of EoS for cold  $\beta$ -equilibrated matter (as it occurs in older compact stars) to finite temperatures and matter out of  $\beta$ -equilibrium as needed for the description of CCSN, PNS evolution,

and BNS mergers. In particular, our finite-temperature EoS models include heavy baryon degrees of freedom - the full baryon octet and  $\Delta$ -resonances. Our EoS model is consistent with available constraints from nuclear physics experiments, *ab initio* calculations of low-density neutron matter, and observations of compact stars, specifically, massive neutron stars, radius and mass inferences by NICER experiment and tidal deformability derived from GW170817 event. We plan to make tables of the EoS publicly available on the Compose database.

As discussed previously for cold compact stars (Drago et al. 2014; Li et al. 2018), the population of  $\Delta$ s at intermediate densities, before the onset of most hyperons, leads to smaller radii for intermediate-mass stars. The impact on the maximum mass compared with hypernuclear models is nevertheless negligible since at high densities anyway many different states are populated and the additional  $\Delta$  degree of freedom only leads to a rearrangement of par-

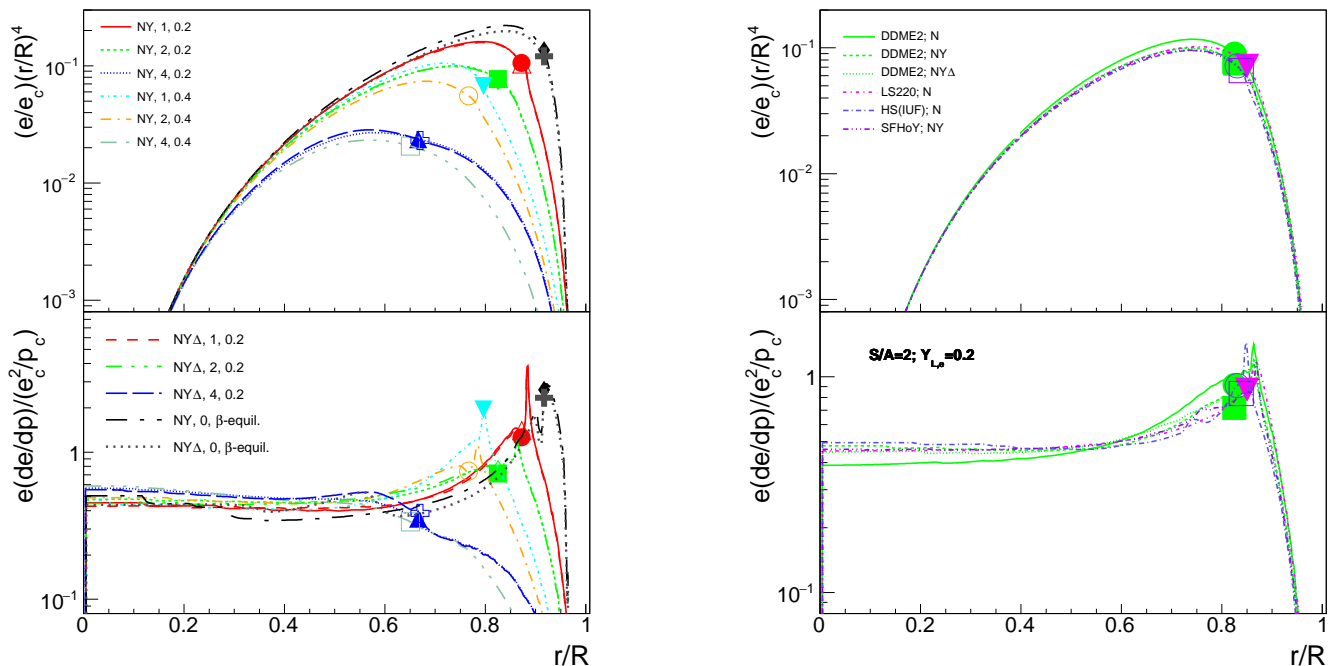


**Figure 14.** Normalised radial profiles of  $(e/e_c)(r/R)^4$  (top panels) and  $e(de/dp)/(e_c^2/p_c)$  (bottom panels) for stars with compactness  $C = 0.17$ , as predicted by various EoS models. Left panels illustrate results corresponding to DDME2( $Y\Delta$ ) model for various thermodynamic conditions specified in the legend in terms of  $(S/A, Y_{L,e})$ ; the label “0,  $\beta$ -equil.” corresponds to cold catalyzed neutrino-transparent matter. Right panels illustrate results corresponding to different EoS models and matter compositions ( $N, NY, NY\Delta$ ) for  $(S/A = 2, Y_{L,e} = 0.2)$ . The crust-core transition is indicated, in each case, by a symbol.

ticle abundances. As long as no additional degrees of freedom are populated, *thermal effects lead to an increase of the maximum gravitational mass with  $S/A$* . This is particularly the case of purely nucleonic stars and hypernuclear stars at high temperatures. The population of additional particle degrees of freedom by thermal excitation can, on the other hand, reduce the maximum gravitational mass with increasing  $S/A$ . The lepton fraction modifies the star’s maximum gravitational mass, too. Depending on the EoS,  $S/A$ , and particle degrees of freedom, compact star’s maximum gravitational mass may increase or decrease with the lepton fraction. Most frequently the gravitational mass of a compact star with an admixture of heavy baryons increases with the lepton fraction, while the opposite effect is obtained for purely nucleonic stars. The reason is that an increasing charge fraction decreases the charge chemical potential and thus disfavors the appearance of, in particular negatively charged, hyperons and  $\Delta$ s. Because of an extended surface, stars at finite temperature and/or high lepton fractions are less compact and less bound than their counterparts at zero temperature. The maximum baryonic mass of a hot star determines the stability against collapse to a black hole. We have shown that, depending on the nuclear EoS, both purely nucleonic stars, and hypernuclear stars may be stable (unstable) within the considered domain of entropy per baryon.

Several authors (Martinon et al. 2014; Marques et al. 2017; Lenka et al. 2019) have argued that thermal effects induce deviations from the universal relations. These findings were confirmed by comparing the relations between various global properties of compact stars at finite  $S/A$  with those at zero temperature. As a byproduct, we have shown that

the  $\Delta$  degrees of freedom do not alter universal relations for cold compact stars. Finally, we have demonstrated that *when the universal relations are studied at the same entropy per baryon and the same lepton fraction, universality is recovered*. We have illustrated this by establishing universal relations between compact star’s compactness and several other global properties as well as by testing the validity of universality for the  $I$ –Love– $Q$  relations. This EoS independence could be helpful for the analysis of observational data from hot, transient states of compact stars, in full analogy to the zero temperature case discussed extensively in the literature. Our findings may also give new hints for the understanding of the origin(s) of universality.

## ACKNOWLEDGMENTS

This work has been partially funded by the European COST Action CA16214 PHAROS “The multi-messenger physics and astrophysics of neutron stars”. A. R. R. acknowledges the hospitality of the Frankfurt Institute for Advanced Studies. A. S. acknowledges the support by the Deutsche Forschungsgemeinschaft (Grant No. SE 1836/5-1) and the hospitality of the Observatoire de Paris, Meudon.

## APPENDIX: UNCERTAINTIES IN RADII OF COMPACT STARS

To quantify the uncertainties related to the surface definition and the crust-core transition we consider four different

case	$n_{min}$	$n_t$	$n_B$ fit domain
(1)	$n_{ll}$	$n_s/3$	-
(2)	$n_{ll}$	$2n_s/3$	-
(3)	$10^{-15}$ [fm $^{-3}$ ]	$n_s/2$	$(n_{ll}, n_t)$
(4)	$10^{-15}$ [fm $^{-3}$ ]	$n_s/2$	$(n_{ll}, n_{LIN})$

**Table 1.** Definition of NS surface and matching between crust and core.  $n_{min}$  defines the baryon number density at the star’s surface,  $n_t$  the transition density from core to crust,  $n_{ll}$  the lowest density in the EoS data tables for the given conditions and  $n_{LIN}$  the maximum density for which  $\log(e) - \log(n_B)$  and  $\log(P) - \log(n_B)$  show a linear behavior to a very good precision between  $n_{ll}$  and  $n_{LIN}$ ;  $n_s$  stands for the saturation density of symmetric nuclear matter.

scenarios, see Table 1. We thereby vary on the one hand the (fixed) transition density from the core to the crust and on the other hand the density at which we define the surface of the star, implying an EoS extrapolation for cases (3) and (4). The top panels of Fig. 1 illustrate, for each scenario, the total pressure as a function of the total energy density together with the EoS data from the Compose database. For this example, the DD2Y EoS (Marques et al. 2017) has been chosen. The bottom panels depict the mass-radius relation, where the cases ( $S/A = 2, Y_{L,e} = 0.2$ ) (left) and ( $S/A = 4, Y_{L,e} = 0.2$ ) (right) have been considered.

As indicated in the main text, we find that: i) the uncertainties related to the arbitrarily chosen value of the crust-core transition density  $n_t$  are negligible, ii) the uncertainties related to the surface definition are sizeable only for stars with high values of  $S/A \gtrsim 3$ . For the shown example, at  $S/A = 4, Y_{L,e} = 0.2$ , the uncertainty in the radius of a 1.4  $M_\odot$  star amounts to 20%. This indicates an upper limit on the uncertainty; for all other studied star properties, the uncertainty is smaller. Similar uncertainties are found for other EoS models, showing that our results are robust.

## REFERENCES

- Abbott B. P., et al., 2017, *Phys. Rev. Lett.*, 119, 161101  
 Abbott B. P., et al., 2018, *Phys. Rev. Lett.*, 121, 161101  
 Abbott B. P., et al., 2019, *Phys. Rev. X*, 9, 011001  
 Antoniadis J., et al., 2013, *Science*, 340, 448  
 Arzoumanian Z., et al., 2018, *ApJ Suppl.*, 235, 37  
 Bailoit d’Etivaux N., Guillot S., Margueron J., Webb N., Catelan M., Reisenegger A., 2019, *ApJ*, 887, 48  
 Baiotti L., Rezzolla L., 2017, *Rep. Prog. Phys.*, 80, 096901  
 Baumgarte T. W., Shapiro S. L., Shibata M., 2000, *ApJ*, 528, L29  
 Bauswein A., 2019, *Ann. Phys. (NY)*, 411, 167958  
 Bauswein A., Janka H., Hebeler K., Schwenk A., 2012, *Phys. Rev. D*, 86, 063001  
 Bejger M., Bulik T., Haensel P., 2005, *MNRAS*, 364, 635  
 Beznogov M. V., Yakovlev D. G., 2015, *MNRAS*, 447, 1598  
 Beznogov M. V., Rrapaj E., Page D., Reddy S., 2018, *Phys. Rev. C*, 98, 035802  
 Bombaci I., 1996, *A&A*, 305, 871  
 Bonanno L., Sedrakian A., 2012, *A&A*, 539, A16  
 Breu C., Rezzolla L., 2016, *MNRAS*, 459, 646  
 Burrows A., Lattimer J. M., 1986, *ApJ*, 307, 178  
 Burrows A., Radice D., Vartanyan D., Nagakura H., Skinner M. A., Dolence J. C., 2020, *MNRAS*, 491, 2715  
 Cai B.-J., Fattoyev F. J., Li B.-A., Newton W. G., 2015, *Phys. Rev. C*, 92, 015802  
 Chatterjee D., Vidana I., 2016, *Eur. Phys. J.*, A52, 29  
 Chen Y., Guo H., Liu Y., 2007, *Phys. Rev. C*, 75, 035806

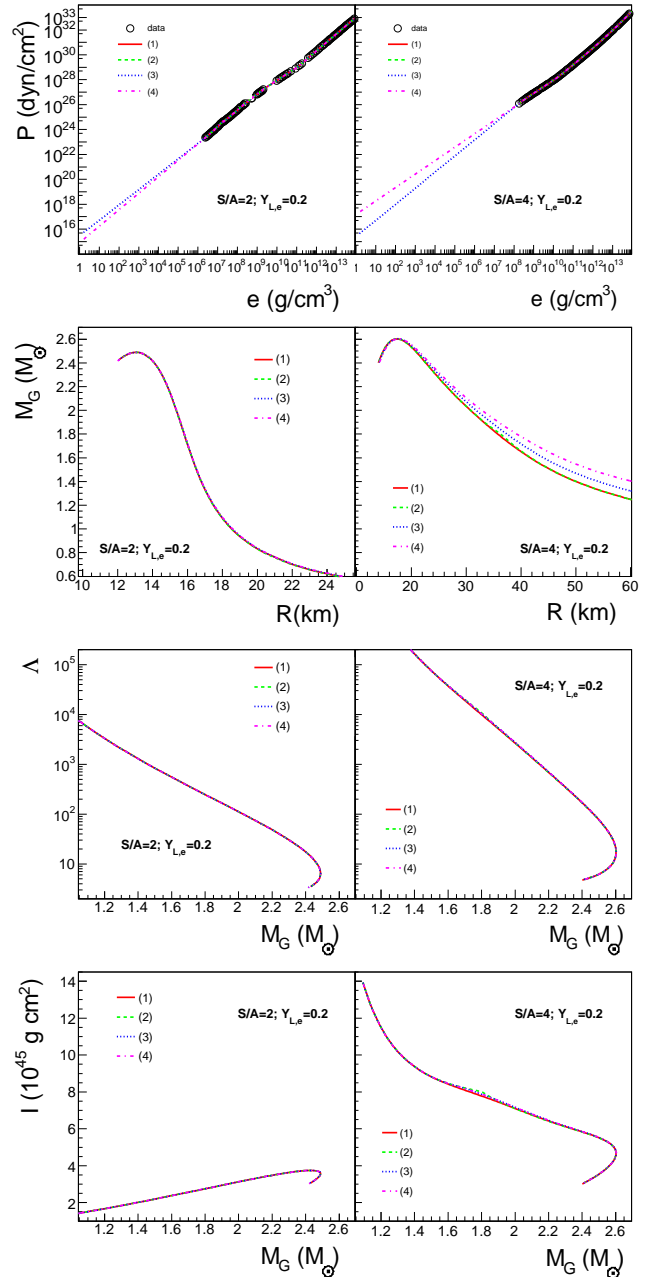


**Figure 1.** EoS (1st row) and relations between gravitational mass and radius (2nd row), tidal deformability and gravitational mass (3rd row) and moment of inertia and gravitational mass (4th row) for non-rotating stars comparing different definitions of NS’s surface and the crust-core transition as listed in Table 1. For the thermodynamic conditions, ( $S/A = 2, Y_{L,e} = 0.2$ ) (left panels) and ( $S/A = 4, Y_{L,e} = 0.2$ ) (right panels) have been chosen. The open circles marked as “data” indicate the EoS data from the Compose database corresponding to the DD2Y EoS (Marques et al. 2017).

- Colucci G., Sedrakian A., 2013, *Phys. Rev. C*, 87, 055806  
 Demorest P. B., Pennucci T., Ransom S. M., Roberts M. S. E., Hessels J. W. T., 2010, *Nature*, 467, 1081  
 Dexheimer V., 2017, *Publ. Astron. Soc. Austral.*, 34, e066  
 Doneva D. D., Yazadjiev S. S., Stergioulas N., Kokkotas K. D., 2013, *ApJ*, 781, L6  
 Drago A., Lavagno A., Pagliara G., Pigato D., 2014,

- Phys. Rev. C*, 90, 065809
- Ducoin C., Chomaz P., Gulminelli F., 2007, *Nucl. Phys. A*, 789, 403
- Ducoin C., Providencia C., Santos A. M., Brito L., Chomaz P., 2008, *Phys. Rev. C*, 78, 055801
- Fattoyev F. J., Horowitz C. J., Piekarewicz J., Shen G., 2010, *Phys. Rev. C*, 82, 055803
- Fischer T., Whitehouse S., Mezzacappa A., Thielemann F.-K., Liebendorfer M., 2009, *A&A*, 499, 1
- Fischer T., Hempel M., Sagert I., Suwa Y., Schaffner-Bielich J., 2014, *Eur. Phys. J. A*, 50, 46
- Fortin M., Providência C., Raduta A. R., Gulminelli F., Zdunik J. L., Haensel P., Bejger M., 2016, *Phys. Rev. C*, 94, 035804
- Fortin M., Avancini S. S., Providência C., Vidaña I., 2017, *Phys. Rev. C*, 95, 065803
- Fortin M., Oertel M., Providência C., 2018, *Publ. Astron. Soc. Austral.*, 35, 44
- Fortin M., Raduta A. R., Avancini S., Providência C. m. c., 2020, *Phys. Rev. D*, 101, 034017
- Gal A., Hungerford E. V., Millener D. J., 2016, *Rev. Mod. Phys.*, 88, 035004
- Gandolfi S., Carlson J., Reddy S., 2012, *Phys. Rev. C*, 85, 032801
- Glendenning N. K., 1985, *ApJ*, 293, 470
- Gourgoulhon E., Grandclement P., Marck J.-A., Novak J., Taniguchi K., 2016, Astrophysics Source Code Library
- Goussard J. O., Haensel P., Zdunik J. L., 1998, *A&A*, 330, 1005
- Grigorian H., Voskresensky D., Maslov K., 2018, *Nucl. Phys. A*, 980, 105
- Gulminelli F., Raduta A. R., 2015, *Phys. Rev. C*, 92, 055803
- Gusakov M. E., Haensel P., Kantor E. M., 2014, *MNRAS*, 439, 318
- Hartle J. B., 1967, *ApJ*, 150, 1005
- Hebeler K., Lattimer J. M., Pethick C. J., Schwenk A., 2013, *ApJ*, 773, 11
- Hempel M., Schaffner-Bielich J., 2010, *Nucl. Phys. A*, 837, 210
- Hempel M., Fischer T., Schaffner-Bielich J., Liebendorfer M., 2012, *ApJ*, 748, 70
- Hess D., Sedrakian A., 2011, *Phys. Rev.*, D84, 063015
- Hinderer T., 2008, *ApJ*, 677, 1216
- Hinderer T., Lackey B. D., Lang R. N., Read J. S., 2010, *Phys. Rev. D*, 81, 123016
- Janka H.-T., Langanke K., Marek A., Martinez-Pinedo G., Mueller B., 2007, *Phys. Rep.*, 442, 38
- Jiang N., Yagi K., 2020, submitted
- Kaplan J. D., Ott C. D., O'Connor E. P., Kiuchi K., Roberts L., Duez M., 2014, *ApJ*, 790, 19
- Kastaun W., Galeazzi F., 2015, *Phys. Rev. D*, 91, 064027
- Koch J., Ohtsuka N., 1985, *Nucl. Phys. A*, 435, 765
- Kolomeitsev E., Maslov K., Voskresensky D., 2017, *Nuclear Physics A*, 961, 106
- Lalazissis G. A., Nikšić T., Vretenar D., Ring P., 2005, *Phys. Rev. C*, 71, 024312
- Lattimer J. M., Prakash M., 2001, *ApJ*, 550, 426
- Lattimer J. M., Schutz B. F., 2005, *ApJ*, 629, 979
- Lattimer J. M., Steiner A. W., 2014, *Eur. Phys. J. A*, 50, 40
- Lattimer J. M., Swesty F. D., 1991, *Nucl. Phys. A*, 535, 331
- Leinson L. B., 2019, *J. Cosmology Astropart. Phys.*, 2019, 031
- Lenka S. S., Char P., Banik S., 2019, *Journal of Physics G: Nuclear and Particle Physics*, 46, 105201
- Li J. J., Sedrakian A., 2019a, *Phys. Rev. C*, 100, 015809
- Li J. J., Sedrakian A., 2019b, *ApJ Lett.*, 874, L22
- Li J. J., Sedrakian A., Weber F., 2018, *Phys. Lett. B*, 783, 234
- Li J. J., Sedrakian A., Alford M., 2020, *Phys. Rev. D*, 101, 063022
- Malfatti G., Orsaria M. G., Contrera G. A., Weber F., Ranea-Sandoval I. F., 2019, *Phys. Rev. C*, 100, 015803
- Marques M., Oertel M., Hempel M., Novak J., 2017, *Phys. Rev. C*, 96, 045806
- Martinon G., Maselli A., Gualtieri L., Ferrari V., 2014, *Phys. Rev. D*, 90, 064026
- Maselli A., Cardoso V., Ferrari V., Gualtieri L., Pani P., 2013, *Phys. Rev. D*, 88, 023007
- Mezzacappa A., et al., 2015, arXiv e-prints, p. [arXiv:1507.05680](https://arxiv.org/abs/1507.05680)
- Miller M. C., et al., 2019, *ApJ Lett.*, 887, L24
- Miyatsu T., Cheoun M.-K., Saito K., 2013, *Phys. Rev. C*, 88, 015802
- Mondal C., Agrawal B. K., De J. N., Samaddar S. K., Centelles M., Viñas X., 2017, *Phys. Rev. C*, 96, 021302
- Morrison I. A., Baumgarte T. W., Shapiro S. L., 2004, *ApJ*, 610, 941
- Most E. R., Weih L. R., Rezzolla L., Schaffner-Bielich J., 2018, *Phys. Rev. Lett.*, 120, 261103
- Nakamura S. X., Sato T., Lee T.-S. H., Szczerbinska B., Kubodera K., 2010, *Phys. Rev. C*, 81, 035502
- Negreiros R., Tolos L., Centelles M., Ramos A., Dexheimer V., 2018, *ApJ*, 863, 104
- O'Connor E. P., Couch S. M., 2018, *ApJ*, 865, 81
- O'Connor E., Ott C. D., 2011, *Astrophys. J.*, 730, 70
- Oertel M., Fantina A. F., Novak J., 2012, *Phys. Rev. C*, 85, 055806
- Oertel M., Providência C., Gulminelli F., Raduta A. R., 2015, *J. Phys. G*, 42, 075202
- Oertel M., Gulminelli F., Providência C., Raduta A. R., 2016, *Eur. Phys. J.*, A52, 50
- Oertel M., Hempel M., Klahn T., Typel S., 2017, *Rev. Mod. Phys.*, 89, 015007
- Ouellette S. M., 2011, PhD thesis, Caltech ([arXiv:hep-ph/0101055](https://arxiv.org/abs/hep-ph/0101055))
- Page D., Lattimer J. M., Prakash M., Steiner A. W., 2004, *ApJ Suppl.*, 155, 623
- Page D., Lattimer J. M., Prakash M., Steiner A. W., 2009, *ApJ*, 707, 1131
- Pais H., Santos A., Brito L., Providencia C., 2010, *Phys. Rev. C*, 82, 025801
- Paschalidis V., Yagi K., Alvarez-Castillo D., Blaschke D. B., Sedrakian A., 2018, *Phys. Rev.*, D97, 084038
- Perego A., Bernuzzi S., Radice D., 2019, *Eur. Phys. J. A*, 55, 124
- Peres B., Oertel M., Novak J., 2013, *Phys. Rev. D*, 87, 043006
- Pons J. A., Reddy S., Prakash M., Lattimer J. M., Miralles J. A., 1999, *ApJ*, 513, 780
- Postnikov S., Prakash M., Lattimer J. M., 2010, *Phys. Rev. D*, 82, 024016
- Prakash M., Bombaci I., Prakash M., Ellis P. J., Lattimer J. M., Knorren R., 1997, *Phys. Rep.*, 280, 1
- Raaijmakers G., et al., 2019, submitted
- Raduta A. R., Gulminelli F., 2010, *Phys. Rev. C*, 82, 065801
- Raduta A. R., Sedrakian A., Weber F., 2018, *MNRAS*, 475, 4347
- Raduta A. R., Li J. J., Sedrakian A., Weber F., 2019, *MNRAS*, 487, 2639
- Ravenhall D. G., Pethick C. J., 1994, *ApJ*, 424, 846
- Ribes P., Ramos A., Tolos L., Gonzalez-Boquera C., Centelles M., 2019, *ApJ*, 883, 168
- Riley T. E., et al., 2019, *ApJ Lett.*, 887, L21
- Rosswog S., 2015, *Int. J. Mod. Phys. D*, 24, 30012
- Ruiz M., Tsokaros A., Shapiro S. L., 2020, *Phys. Rev. D*, 101, 064042
- Sahoo H. S., Mitra G., Mishra R., Panda P. K., Li B.-A., 2018, *Phys. Rev. C*, 98, 045801
- Sawyer R. F., 1972, *ApJ*, 176, 205
- Schneider A., Roberts L., Ott C., O'Connor E., 2019, *Phys. Rev. C*, 100, 055802
- Schneider A. S., O'Connor E., Granqvist E., Betranhandy A., Couch S. M., 2020, submitted
- Sedrakian A., 2016a, *Eur. Phys. J.*, A52, 44
- Sedrakian A., 2016b, *Phys. Rev.*, D93, 065044
- Sedrakian A., 2019, *Phys. Rev.*, D99, 043011

- Sedrakian A., Clark J. W., 2019, *Eur. Phys. J. A*, **55**, 167
- Sekiguchi Y., Kiuchi K., Kyutoku K., Shibata M., 2011, *Phys. Rev. Lett.*, **107**, 211101
- Shibata M., Taniguchi K., 2011, *Living Rev.Rel.*, **14**, 6
- Sorkin R. D., 1982, *ApJ*, **257**, 847
- Spinella W., 2017, PhD thesis, Claremont Graduate University/San Diego State University
- Steiner A. W., Lattimer J. M., Brown E. F., 2010, *ApJ*, **722**, 33
- Steiner A. W., Hempel M., Fischer T., 2013, *ApJ*, **774**, 17
- Stone J. R., Dexheimer V., Guichon P. A. M., Thomas A. W., 2019, submitted
- Sumiyoshi K., Yamada S., Suzuki H., 2007, *ApJ*, **667**, 382
- Tolos L., Centelles M., Ramos A., 2016, *ApJ*, **834**, 3
- Tolos L., Centelles M., Ramos A., 2017, *Publ. Astron. Soc. Austral.*, **34**, e065
- Typel S., Röpke G., Klähn T., Blaschke D., Wolter H. H., 2010, *Phys. Rev. C*, **81**, 015803
- Typel S., Oertel M., Klähn T., 2015, *Phys. Part. Nucl.*, **46**, 633
- Wehrberger K., Bedau C., Beck F., 1989, *Nucl. Phys. A*, **504**, 797
- Wei J.-B., Burgio G., Schulze H.-J., 2019, *MNRAS*, **484**, 5162
- Wei J. B., Burgio G. F., Schulze H. J., 2020, arXiv e-prints, [p. arXiv:2003.08079](https://arxiv.org/abs/2003.08079)
- Weissenborn S., Chatterjee D., Schaffner-Bielich J., 2012a, *Phys. Rev. C*, **85**, 065802
- Weissenborn S., Chatterjee D., Schaffner-Bielich J., 2012b, *Nucl. Phys. A*, **881**, 62
- Yagi K., Yunes N., 2013a, *Phys. Rev. D*, **88**, 023009
- Yagi K., Yunes N., 2013b, *Science*, **341**, 365
- Yagi K., Yunes N., 2017, *Phys. Rep.*, **681**, 1
- Yasin H., SchÄdfer S., Arcones A., Schwenk A., 2020, *Phys. Rev. Lett.*, **124**, 092701
- Zhu Z.-Y., Li A., Hu J.-N., Sagawa H., 2016, *Phys. Rev. C*, **94**, 045803
- Zimmerman J., Carson Z., Schumacher K., Steiner A. W., Yagi K., 2020, submitted
- de Carvalho S. M., Negreiros R., Orsaria M., Contrera G. A., Weber F., Spinella W., 2015, *Phys. Rev.*, **C92**, 035810
- van Dalen E. N. E., Colucci G., Sedrakian A., 2014, *Phys. Lett. B*, **734**, 383